remote sensing

MDPI

Article

Pre-Processing of Simulated Synthetic Aperture Radar Image Scenes Using Polarimetric Enhancement for Improved Ship Wake Detection

Yanni Jiang, Ziyuan Yang, Ke Li and Tao Liu *

School of Electronic Engineering, Naval University of Engineering, Wuhan 430033, China; asiajiang2005@163.com (Y.J.); yzy_199702@sina.com (Z.Y.); michael_lee0702@163.com (K.L.)
* Correspondence: liutao1018@hotmail.com

Abstract: Ship wake detection using synthetic aperture radar (SAR) imagery provides a way to obtain small marine ship information, but it often becomes unavailable and unreliable during a high sea state. Polarimetric information provides a potential way to solve this problem, which can enhance the ship target as well as the ship wake features. However, three challenges still exist in ship wake detection in polarimetric SAR imagery: the unwanted influences of bright and singular points on ship wake detection, the lack of performance analysis of wake detection by new-type polarimetric enhancement methods, and the difficulty of using the assessment criteria for ship wake detection. In this paper, we try to solve the above problems. Firstly, fully polarized SAR imagery of both ship turbulent and Kelvin wake is simulated based on the two-scale composite model, and the Polarimetric Whitening Filter (PWF) and Polarimetric Detection Optimization Filter (PDOF) are applied to the simulated fully polarized SAR imagery to enhance the ship wake features. Secondly, since the bright and singular points resulting from the ship echoes and the polarimetric enhancement methods may lead to misdetections, a logarithm process and z-score normalization pre-processing has been applied to the images. Then, a new assessment criterion for wake detection performance has been formulated, and the probability of missing detections (PMDs) and the probability of false alarms (PFAs) have been defined for two different requirements. And a Radon transform-based ship wake detection method for both ship turbulence and Kelvin wake has been carried out in horizontal–horizontal (HH), vertical–vertical (VV), horizontal–vertical (HV), PWF and PDOF SAR imagery. Finally, an analysis of the wake detection performance has been carried out. The PWF and PDOF can improve the wake detection performance by an average of nearly 50 percent compared with the HH and VV.

Keywords: ship wake simulation; ship wake detection; polarimetric SAR (PolSAR); Polarimetric Whitening Filter (PWF); Polarimetric Detection Optimization Filter (PDOF)

check for updates

Citation: Jiang, Y.; Yang, Z.; Li, K.; Liu, T. Pre-Processing of Simulated Synthetic Aperture Radar Image Scenes Using Polarimetric Enhancement for Improved Ship Wake Detection. *Remote Sens.* **2024**, *16*, 658. https://doi.org/10.3390/rs16040658

Academic Editor: Domenico Velotto

Received: 14 December 2023
Revised: 7 February 2024
Accepted: 9 February 2024
Published: 11 February 2024

Copyright: © 2024 by the authors. Licensee MDPI, Basel, Switzerland. This article is an open access article distributed under the terms and conditions of the Creative Commons Attribution (CC BY) license (https://creativecommons.org/licenses/by/4.0/).

1. Introduction

Detecting ship wake features in synthetic aperture radar (SAR) imagery can provide an alternative way to obtain marine ship information, but it often becomes unavailable and unreliable for small, high-speed and stealthy marine ship targets during a high sea state [1]. Polarimetric SAR (PolSAR) can characterize the polarimetric properties of target backscatter and enhance the ship wake features, therefore it provides a potential way to solve this problem.

Since the 1990s, researchers have been exploiting the potential of utilizing the polarimetric signatures of the ship wake features. D.L. Schuler et al. [2] studied the full PolSAR signatures of ocean surface features and ship wakes. E. Pottier et al. [3] applied an unsupervised classification procedure based on neural networks to the full PolSAR imagery of sea surface and ship wakes for segmentation and the clustering of different ocean components. D. Kasilingam et al. [4] investigated the modulation of full PolSAR imagery through large oceanic features including ship wake. J. Morris et al. [5,6] addressed the problem of ship

wake detection and analysis at low grazing angles using an eigenvalue analysis of the covariance matrix, and demonstrated that wake feature extraction and discrimination can be achieved in the polarisation domain. J. Yang et al. [7] used full PolSAR data collected by AIRSAR and SIR-C/X-SAR to analyse radar signatures of ocean features including ship wakes. P. Wu et al. [8] extracted and studied the polarimetric character of the Kelvin wakes for the detection or identification of the wakes based on the difference in scattering mechanism between Kelvin wakes and sea clutter in SAR imagery, with multiband and full polarization.

Later researchers have devoted great effort to utilizing the polarimetric information to enlarge the difference of ship wake and the background. Many optimal methods for polarimetric detection have been proposed, such as the Optimal Polarimetric Detector (OPD) [9,10], the Polarimetric Notch Filter (PNF) [11] and the Polarimetric Whitening Filter (PWF) [12]. P. Imbo et al. [13] described two methods for wake-shape detection in PolSAR imagery: the first one reduced the dimension of the scattering matrix using the PWF filter, which can improve the contrast between ships and sea clutter in the background; the second one utilized the covariance matrix in the Radon domain. Z. Xu et al. [14] introduced a novel two-step (coarse and fine processing) detector to detect the faint turbulent wake in PolSAR imagery. Based on the polarization decomposition theory, a new parameter called surface scattering randomness was proposed to enhance the contrast between wake and sea. F. Biondi et al. [15,16] proposed an algorithm consisting of considering the polarimetric information of SAR imagery and evaluating a multiple-channel and dual-stage Pol low-rank plus sparse decomposition assisted by the Radon transform for clutter reduction, sparse object detection, precise wake inclination estimation and target classification. T. Liu proposed the Polarimetric Detection Optimization Filter (PDOF) [17] to maximize the ratio of target clutter ratio over the speckle for ship detection in PolSAR imagery. And the simulated and real experiments showed that the PDOF detector is effective and robust, and can provide a performance which is similar to those of the best traditional detectors. Most of the polarimetric enhancement methods are often applied to ship detection [18–22]; however, the potential of the polarimetric enhancement method in ship wake detection still needs to be discovered.

The measured full-polarized dataset for ship and ship wake is often lacking in practice, and the simulated data can provide prior information about the ship's parameters [23,24]. Therefore, the ship wake detection algorithm is often validated by the simulated SAR imagery first. For current SAR imaging simulations of the two-scale composite model (TSM), the HH and VV polarization have been considered in most of the occasions. G. Zilman et al. [25] simulated 6750 SAR images of sea surfaces with Kelvin wake embedded in it, including the variations in wind speed, wind direction, ship velocity and ship azimuth angle. And they also analysed the wake detection performance based on these simulated SAR images. Unfortunately, only the HH and VV polarizations have been considered. I.G. Rizaev et al. [26] presented a universal simulation framework for SAR imagery of the sea surface including the superposition of sea-ship waves. They also carried out ship wake detection based on some of the simulated SAR images. Yuxin et al. [23] calculated the electromagnetic scattering characteristics of the turbulent wake using the two-scale facet mode, and considered the HH, HV and VV polarization factors. J. Wang et al. [24] calculated the scattering echo of the Kelvin wake using the two-scale method, and analyzed the influence of various SAR system parameters including polarization on Kelvin wake detection in numerically simulated SAR images. They pointed out that the characteristics of Kelvin wake in SAR images can hardly be seen under the cross-polarization. Recently, we have released a full-polarized Polarized Ship Detection Dataset (FPSD) [27], which contains the full polarimetric information of ship and can be applied to the validation and perfection of the ship wake detection algorithms.

In addition, the lack of mature and uniform criteria makes it hard to assess the performance of ship wake detection of large amount of SAR images. In [25], the probability of missing detections (PMD) and the probability of false alarms (PFA) in Kelvin wake

detection have been defined and analyzed. But it is only suitable for the detection of the two Kelvin wake arms. Tings et al. [28] proposed an extension of the wake detectability model by using a non-linear basis which allows for the consideration of all the influencing parameters simultaneously, which provides new insights and a better understanding of the non-linear influence of parameters on the wake detectability. O. Karakus et al. [29] defined the sensitivity, specificity, accuracy of detecting Kelvin, narrow-V and turbulent wakes, but it has only been applied to a very small amount of images. Tings et al. [30] evaluated the differences in detectability of wake components including the near-hull turbulence, turbulent wake, Kelvin wake arms and V-narrow wakes between four SAR sensors (TerraSAR–X, CosmoSkymed, Sentinel-1 and RADARSAT-2), and quantitative and qualitative analyses were conducted and a measure for the detectability models' uncertainties was introduced. But they only investigated the relative detectability of individual wake components.

Furthermore, the ship echo, land signatures and ship propellers disturbances may appear in the SAR imagery as small areas of extremely bright returns [31]. And their effect on the Radon transform is to swamp the Radon images with very bright sinusoids [15,16], making the detection of wake peaks difficult. The influences of such bright pixels are often removed by some pre-processing methods before the wake detection. M. Rey et al. [32] determined a threshold and used it to detect the pixel values associated with the ship returns, and replaced the area of the original image containing the ship returns with the mean value of the image amplitude. M. Graziano et al. [33] applied a constant false alarm rate (CFAR) approach to form the ship-centered images, and then masked those bright pixels with a rectangular area determined by the prior ship information. O. Karakus et al. [29] applied a two-step pre-processing including the creation of ship-centered and masked images. For the masking operation, when replacing the area of the ship location with the mean intensity, only the unmasked pixels have been taken into account and the area containing the ship and land returns is ignored. These methods require the prior information of ship, and the inappropriate choice of the masked area and replacing value may lead to a degrade of wake detection performances.

To solve the above problems, in this paper, firstly we propose an algorithm for simulating ship turbulent wake and ship Kelvin wake simultaneously in PolSAR imagery of ocean areas, applying the TSM. Secondly, we apply the PWF and PDOF to enhance the wake features in the PolSAR imagery. Then, a logarithm process and a z-score normalization were applied to eliminate the influences of the bright and singular points. After that, a new assessment criterion of wake detection performance has been formulated, and a Radon transform-based ship wake detection has been carried out in the simulated and measured HH, VV, HV, PWF and PDOF images. Finally, an analysis of the wake detection performance has been performed.

The remainder of the paper is organized as follows. The theoretical foundation of ship wake simulation and polarimetric enhancement is demonstrated in Section 2. The methodology is displayed in Section 3. The experimental results and the discussion are displayed in Section 4. Section 5 concludes this paper.

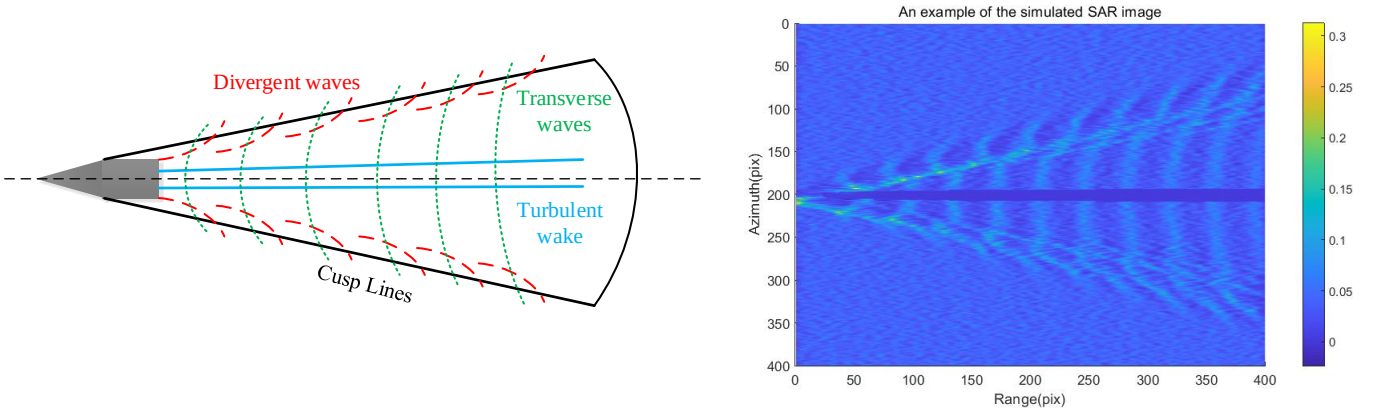
2. Background

2.1. Ship Wake Simulation in SAR Images

Ship wakes in SAR imagery mostly consist of Kelvin wake, turbulent wake, narrow-V wake and internal wake. Among them, the Kelvin wake and turbulent wake are the most likely to appear [34]; the narrow-V wake only appears in SAR imagery in some particular situations. Therefore, this paper mainly focuses on the simulation and detection of the Kelvin wake and turbulent wake, as denoted in Figure 1.

The Kelvin wake [25] can be formed by the superposition of the divergent waves and transverse waves, which form the cusp lines angle θ_C. The boundaries of Kelvin wake appear as a V-angle, and in SAR images the cusp lines angle θ_C is about

$$20^\circ \leq \theta_C \leq 39^\circ \quad (1)$$



(**a**) (**b**)

Figure 1. Kelvin wake and turbulent wake in SAR imagery of sea surfaces. (**a**) Diagrammatic sketch; (**b**) an example of the simulated SAR images.

Applying the Michell thin ship theory, the ship-generated kelvin wake elevation Z_{SK} of the free surface can be represented as a superposition of gravity waves.

The ship turbulent wake consists of the jet wake and the vortex wake. To simplify, only the jet wake is considered in this paper. In SAR imagery, the ship turbulence jet wake causes a strong attenuation of short gravity-capillary waves and usually appears as a dark line after the ship [35]. A semi-empiric relationship between the ship beam B and the width of its turbulent wake after the ship has been derived in [36]:

$$W(x_{DS}) = \overline{\omega}_0 \left(\frac{\overline{x}_0 L}{B} \right)^{-1/\alpha} B^{(\alpha-1)/\alpha} x_{DS}^{1/\alpha} \quad (2)$$

where $\overline{x}_0 \approx 4$ and $\overline{\omega}_0 \approx 4$, α varies between 4 and 5 and x_{DS} is the distance after the ship.

A semi-empirical energy spectrum-based method has been adopted to simulate the wind-driven sea surface and the turbulent wake [37]. Applying the linear superposition method, the wind-driven sea surface height can be represented as the superposition of monochromatic waves of different amplitudes, angular frequencies, water wavenumbers, wave propagation and initial phases. When simulating the wind-driven sea surface Z_{wind}, we use the Pierson–Moskowitz wave spectrum, and for ship turbulent wake Z_{ST}, we use an energy loss spectrum [36].

In this paper, a two-scale composite model (TSM) and the velocity-bunching integral were used to simulate the SAR image of a sea surface, including the ship, Kelvin and turbulent wake [25]. The total wave elevation of free surface can be seen as a superposition of wind-induced waves, ship-induced Kelvin and turbulent wake waves. Considering the RAR and the velocity-bunching mechanisms, the SAR image can be calculated and the mean RCS $\overline{\sigma}(x, y)$ can be described as:

$$\overline{\sigma}(x, y) = 8\pi k_e^2 \cos\mu_i W\left(k_x^0, k_y^0\right) |T_t|^2 \times \left[1 + 2\mathrm{Re} \int M(\mathbf{k}) F_Z(\mathbf{k}) e^{j\mathbf{k}x} d\mathbf{k} \right] \quad (3)$$

where k_e is the electromagnetic wavenumber, μ_i is the local incident angle of electromagnetic waves, $W(\cdot)$ is the short wave spectrum with the Bragg scattering components k_x^0, k_y^0. $F_Z(\mathbf{k})$ is the 2D Fourier transform of the large-scale sea surface Z. T_t is the complex scattering function depending on the polarizations and the relative dielectric constant of the sea water [38]. And for different polarizations it is defined as:

$$\begin{cases} T_{t,HH} = \left[\frac{\sin(\mu_i+s_p)\cos s_p}{\sin\mu_i}\right]^2 \frac{(\varepsilon_r-1)\left[\varepsilon_r\left(1+\sin^2\mu_i\right)-\sin^2\mu_i\right]}{\left[\varepsilon_r\cos\mu_i+\left(\varepsilon_r-\sin^2\mu_i\right)^{1/2}\right]^2} + \left(\frac{\sin s_p}{\sin\mu_i}\right)^2 \frac{\varepsilon_r-1}{\left[\cos\mu_i+\left(\varepsilon_r-\sin^2\mu_i\right)^{1/2}\right]^2} \\ T_{t,VV} = \left[\frac{\sin(\mu_i+s_p)\cos s_p}{\sin\mu_i}\right]^2 \frac{\varepsilon_r-1}{\left[\cos\mu_i+\left(\varepsilon_r-\sin^2\mu_i\right)^{1/2}\right]^2} + \left(\frac{\sin s_p}{\sin\mu_i}\right)^2 \frac{(\varepsilon_r-1)\left[\varepsilon_r\left(1+\sin^2\mu_i\right)-\sin^2\mu_i\right]}{\left[\varepsilon_r\cos\mu_i+\left(\varepsilon_r-\sin^2\mu_i\right)^{1/2}\right]^2} \\ T_{t,HV} = T_{t,VH} = \left[\frac{\sin(\mu_i+s_p)\cos s_p\sin s_p}{\sin\mu_i}\right]\left\{\frac{(\varepsilon_r-1)\left[\varepsilon_r\left(1+\sin^2\mu_i\right)-\sin^2\mu_i\right]}{\left[\varepsilon_r cos\mu_i+\left(\varepsilon_r-\sin^2\mu_i\right)^{1/2}\right]^2} - \frac{\varepsilon_r-1}{\left[\cos\mu_i+\left(\varepsilon_r-\sin^2\mu_i\right)^{1/2}\right]^2}\right\} \end{cases} \quad (4)$$

where S_p is the local slope of large-wave structure. ε_r is the relative dielectric constant of the sea water. $M(\mathbf{k})$ is the modulation transfer function (MTF), or the sum of the hydrodynamic MTF $M_{hydro}(\mathbf{k})$ and tilt MTF $M_{tilt}(\mathbf{k})$. In the previous simulation of TSM, when calculating the tilt MTF, some simplified formulas for HH and VV polarizations have been developed from the measured data and used for calculation [39]:

$$M_{tilt,HH} = \frac{4\cot\theta_r}{1-\sin^2\theta_r}, M_{tilt,VV} = \frac{4\cot\theta_r}{1+\sin^2\theta_r} \quad (5)$$

where θ_r is the nominal radar incidence angle. The calculation of the tilt MTF of HV and VH polarizations is rather complicated. Therefore, in this paper, to simplify the calculation process, the tilt MTF of HV and VH polarizations are set according to the measured full-Polarized SAR imagery [27] as an empirical value. The correctness of this empirical value has been validated by both the simulated and measured data.

2.2. PWF and PDOF Filter

2.2.1. PWF Filter

The polarimetric scattering matrix can be represented as:

$$\mathbf{S} = \begin{bmatrix} S_{HH} & S_{HV} \\ S_{VH} & S_{VV} \end{bmatrix} \quad (6)$$

where S_{xy} represents the complex scattering coefficient with x and y standing for the transmitting polarization and the receiving polarization (H—horizontal linear; V—vertical linear). When the system is monostatic and the reciprocity condition is satisfied, $S_{HV} = S_{VH}$. Then, the scattering vector $\mathbf{k}$ can be defined as

$$\mathbf{k} = \begin{bmatrix} S_{HH} \\ \sqrt{2}S_{HV} \\ S_{VV} \end{bmatrix}. \quad (7)$$

In the multilook case, the covariance matrix describes the full polarization information and is defined as

$$C = \frac{1}{L}\sum_{i=1}^{L} s_i s_i^H \quad (8)$$

where L is the nominal number of looks.

The output after the PWF in PolSAR imagery is defined as follows [9,10]:

$$z_{PWF} = \mathrm{tr}\left(\mathbf{\Sigma}_C^{-1}\mathbf{C}\right) \quad (9)$$

where $\mathbf{\Sigma} = \mathrm{E}\left\{\mathbf{S}\mathbf{S}^H\right\}$ is defined as the expectation of the covariance matrix $\mathbf{C}$, $E(\bullet)$ denotes the expectation operator and the subscript $\mathbf{C}$ refers to clutter. The PWF detector does not need the prior information of the targets.

2.2.2. PDOF Filter

The Polarimetric Detection Optimization Filter (PDOF) [17] maximizes the target clutter ratio over the speckle variation, and its excellent detection performance of ship detection is validated by both simulated and measured data. Its final expression is

$$z_{PDOF} = \mathrm{tr}\left[(\mathbf{\Sigma}_C^{-1}\mathbf{\Sigma}_T\mathbf{\Sigma}_C^{-1})\mathbf{C}\right] \tag{10}$$

where the subscript **C** and **T** refers to clutter and target, respectively. In measured SAR images, we can estimate the polarimetric covariance matrices $\mathbf{\Sigma}_T$, $\mathbf{\Sigma}_C$ by averaging the selected clutter region or ships. In simulated SAR images, $\mathbf{\Sigma}_C$ can be obtained from the simulated SAR image of pure sea surface without wakes under certain sea state. The choose of the prior information of the targets $\mathbf{\Sigma}_T$ mainly depends on the wake detection algorithm, and it is vital to the wake detection performance. In this paper, $\mathbf{\Sigma}_T$ is obtained from the simulated SAR image of ship wake under calm sea state.

3. Methodology

3.1. The Polarimetric Enhancement

The PWF and PDOF can be applied to the simulated fully polarized SAR images to enhance the ship wake character by the full polarimetric information. An example of the simulated fully polarized and polarimetric-enhanced SAR images can be seen in Figure 2. The wind direction is 0°, the wind speed is 6 m/s, the ship velocity is 12 m/s and the ship heading angle is 200°.

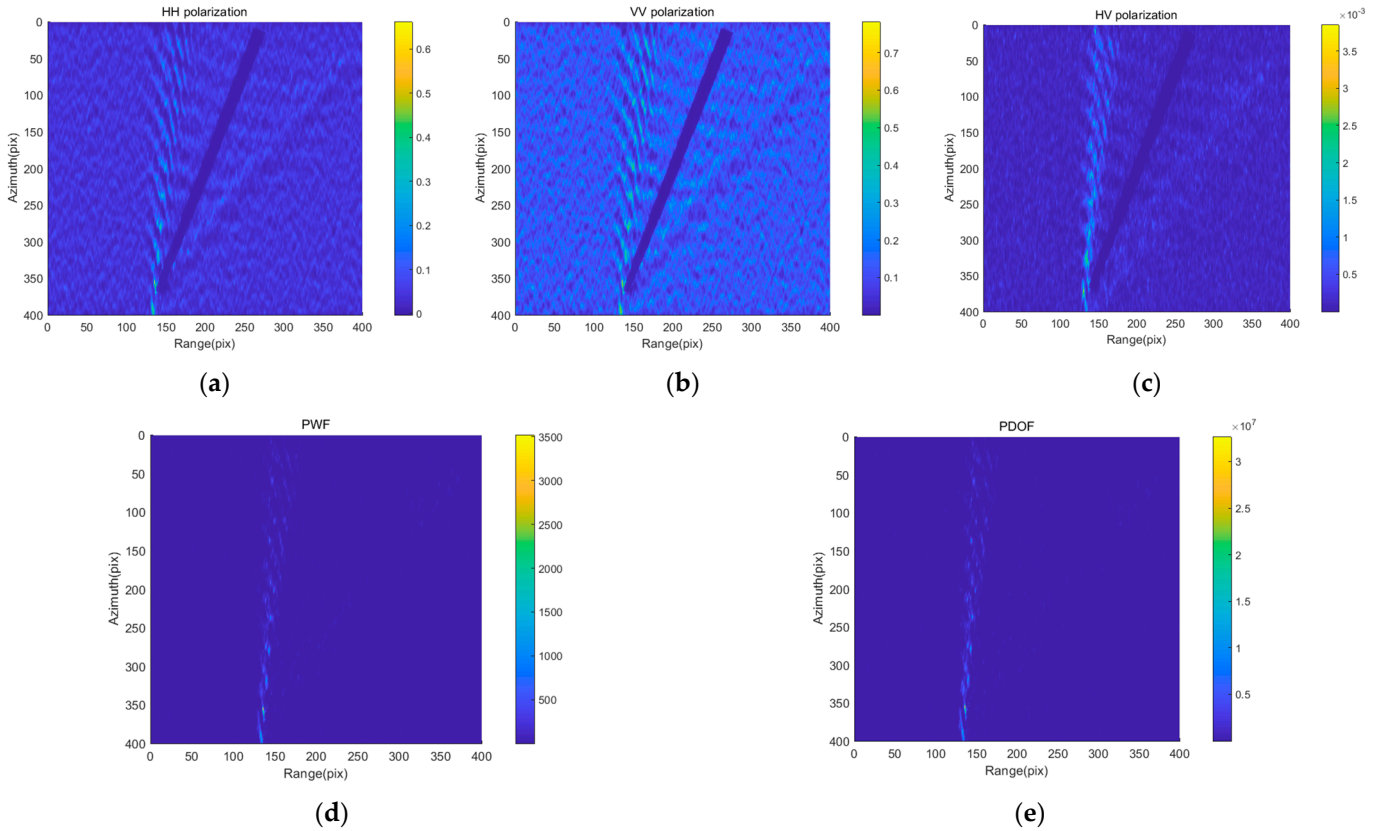


Figure 2. Polarimetric enhancement of the simulated full-polarized SAR images. (**a**) HH; (**b**) VV; (**c**) HV; (**d**) PWF; (**e**) PDOF.

It can be seen that, after PWF filtering, the sea clutter background has been suppressed. After PDOF filtering, the sea clutter has been suppressed, meanwhile the wake characters have been enhanced. However, PWF and PDOF also make the dark turbulent wake

hard to distinguish, and lead to some bright and singular points which may cause wake misdetection. Moreover, PWF and PDOF also enlarge the intensity difference. In Figure 2, the mean image intensity of HH, VV, HV, PWF and PDOF is 0.0435, 0.1218, 0.000146, 7.0247 and 56,475.0000. The image intensity of PFOF is about ten thousand times higher than that of PWF, a million times higher than that of HH and VV and a hundred million times higher than that of HV.

One image has been selected to represent a typical measured SAR imagery in the Fully Polarized Ship Detection Dataset (FPSD), whose number is 00012 [27]. And only the ship and sea clutter are the main components in this image. Since, for the measured data, the prior information of the ship is hard to obtain, only PWF has been carried out here. Pauli pseudo-color maps for HH, VV, HV and PWF SAR images have been listed in Figure 3. The mean image intensities of HH, VV, HV and PWF are 0.0098, 0.0338, 0.000455 and 7.5555, which corresponds to the simulated results very well and can be used to verify the correctness of the simulation.

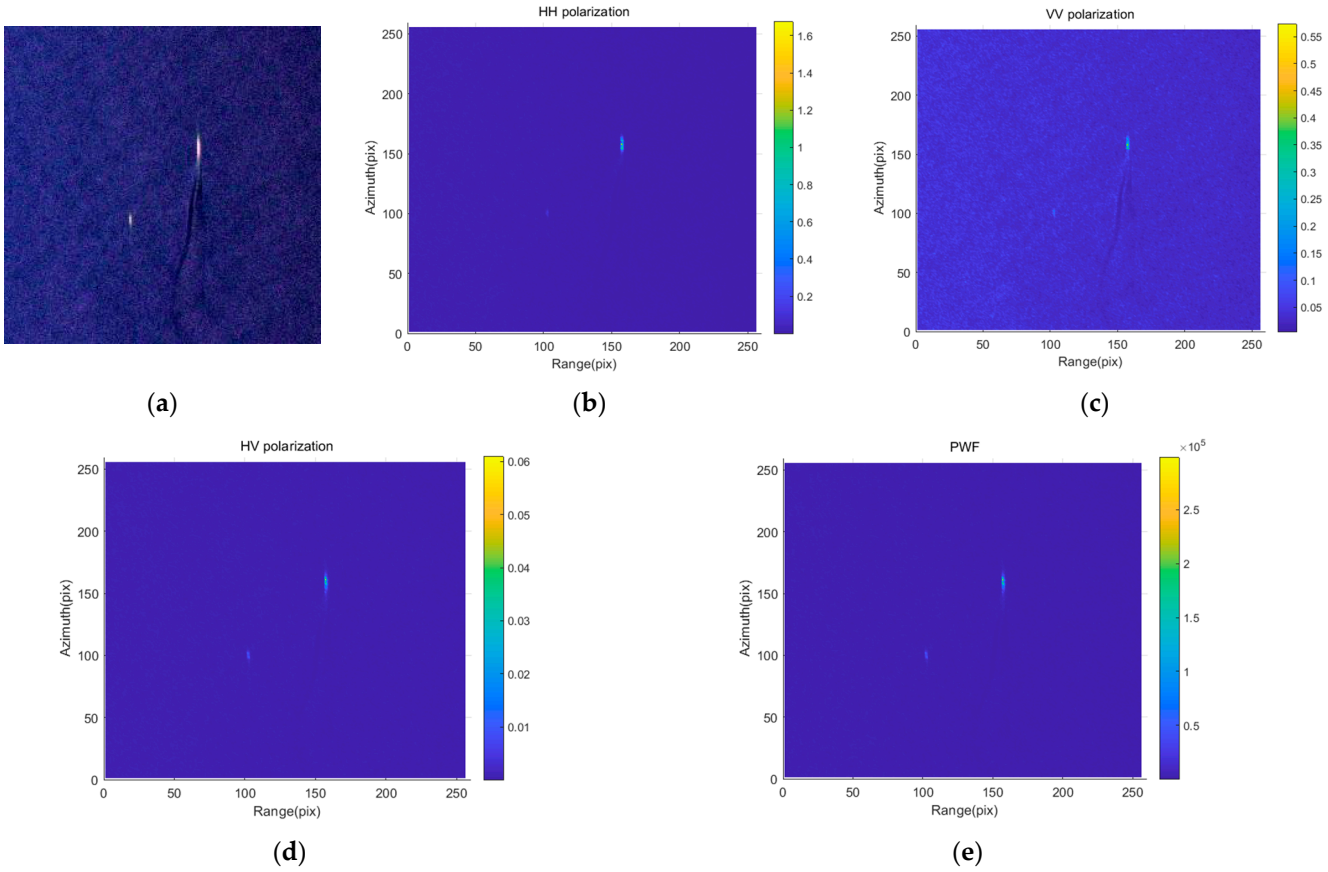


Figure 3. Polarimetric enhancement of the measured full-polarized SAR images in FPDS. (**a**) The Pauli pseudo-color maps; (**b**) HH; (**c**) VV; (**d**) HV; (**e**) PWF.

3.2. The Pre-Processing

The bright and singular points resulting from the ship echoes and the polarimetric enhancement methods may greatly influence the detection of ship wake in the Radon images. To eliminate the uniformity of different polarizations as well as the influence of the singular points in SAR images, a logarithm process and a z-score normalization have been proposed to replace the ship-centered masking process before wake detection. A comparison of the Radon images before and after the pre-process has been displayed in Figure 4. Figure 4a,b are the Radon images of Figures 2d, 3b and 4c,d are their images after the pre-processing. The series of very bright sinusoids in Figure 4a are caused by those bright points in the PWF images (Figure 2d), and they have been darkened through the

pre-processing, resulting in the clear bright and dark clusters in Figure 4c. The two bright sinusoids in Figure 4b are caused by the two bright target echoes in Figure 3b. They have also been largely reduced through the pre-process in Figure 4d, making the bright and dark clusters corresponding to the Kelvin and turbulent wakes more distinguishable.

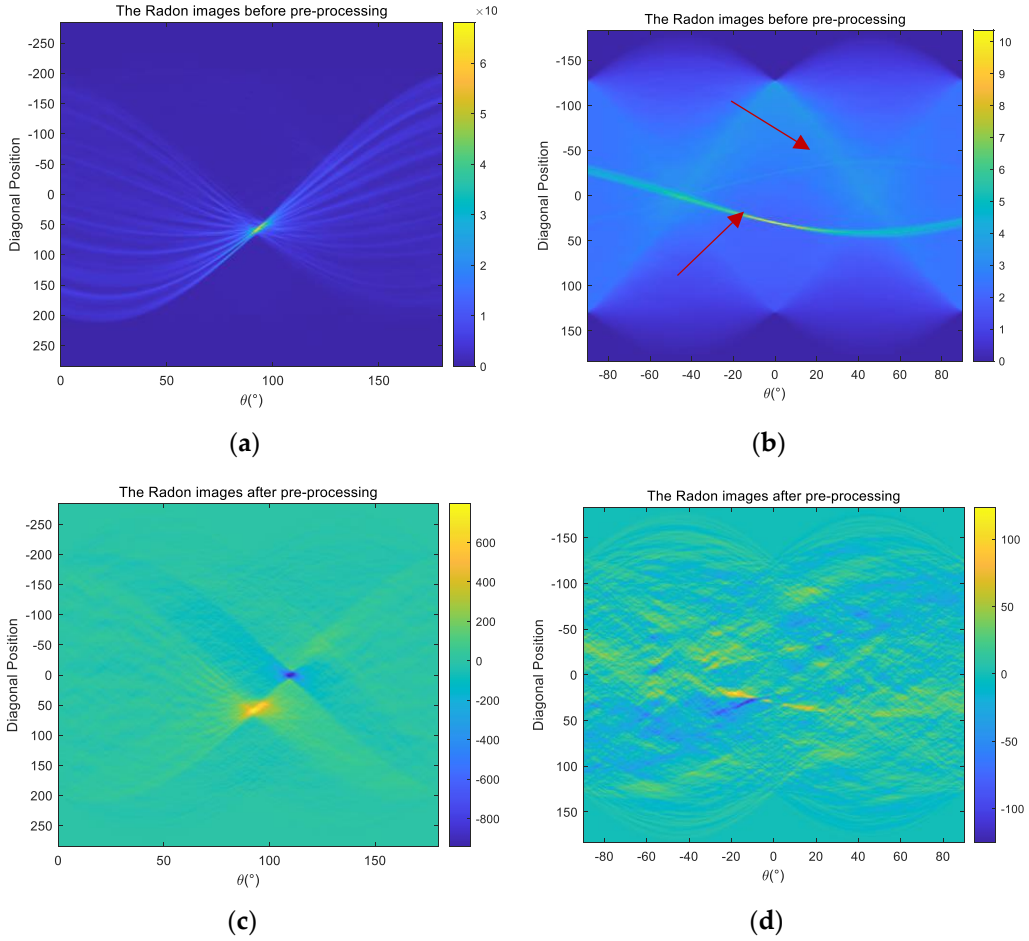


Figure 4. The Radon images before and after the pre−processing. (**a**) The Radon image of Figure 2d; (**b**) the Radon image of Figure 3b; (**c**) the Radon image of Figure 2d after the pre-processing; (**d**) the Radon image of Figure 3b after the pre-processing.

Figure 5 displays an example of the simulated SAR images before and after the pre-processing of HH, VV, HV, PWF and PDOF. The simulation parameters are the same as in Figure 2. Figure 5a,d,g,j,m are the probability distributions of the SAR images of HH, VV, HV, PWF and PDOF before pre-processing. It should be pointed out that the longitudinal coordinates of Figure 5j,m are displayed in logarithmic coordinates in order to amplify the detailed information about probability. Figure 5b,e,h,k,n are the SAR images of HH, VV, HV, PWF and PDOF after pre-processing. Figure 5c,f,i,l,o are the probability distribution of the SAR images of HH, VV, HV, PWF and PDOF after pre-processing, and the red solid lines in these pictures are the Gaussian-fitted curves. After this pre-processing, the image intensities of HH, VV, HV, PWF and PDOF obey a Gauss distribution, and the image intensity differences in HH, VV, HV, PWF and PDOF have almost been reduced. In addition, the dark turbulent wake in the PWF and PDOF images can be distinguished, and the probability of misdetection caused by the singular points is reduced, which make them suitable for the following wake detection procedure and performance assessment.

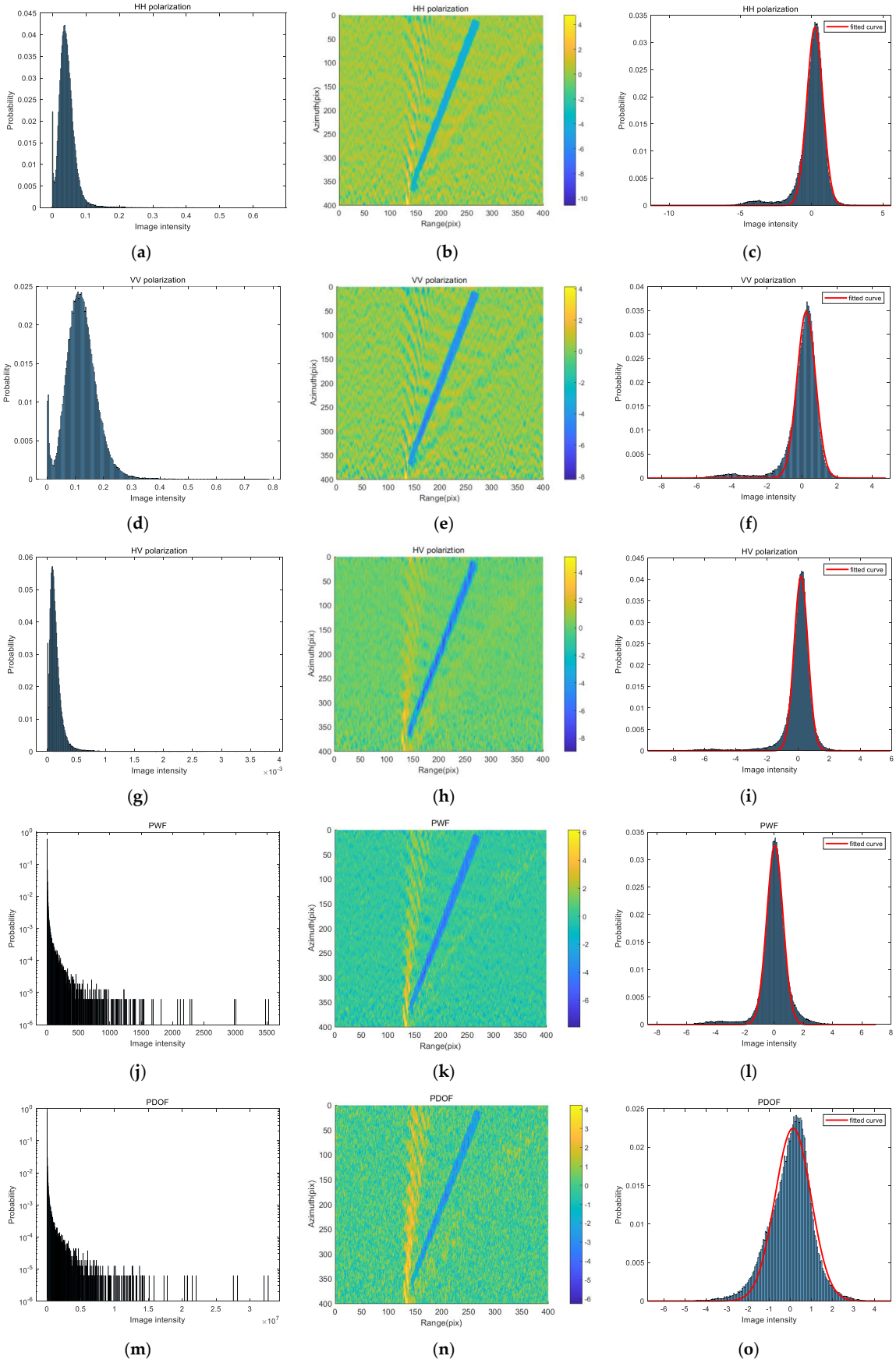


Figure 5. The probability of images, and the simulated SAR images and probability of images after pre−processing. (**a**–**c**) HH; (**d**–**f**) VV; (**g**–**i**) HV; (**j**–**l**) PWF; (**m**–**o**) PDOF.

3.3. The Radon Transform and Detection Procedure

The Radon transform (RT) is adopted to detect the linear features of ship wakes, including the boundaries of both Kelvin wake (the cusp line) and the turbulent wake. A searching method based on the angular positions of Kelvin wake, narrow-V wake and turbulent wake has been addressed in [29,33]. In this paper, only the Kelvin wake and the turbulent wake are considered. For the wake detection, the HH, VV, HV polarizations and the PWF and PDOF share the same procedure.

In the Radon space of the SAR images, the boundaries of Kelvin wake usually appear as two bright or slightly bright clusters. Turbulent wake is the most visible wake character and usually appears as a dark cluster [29], and we assume that it is always surrounded by two Kelvin arms. Therefore, in the Radon space, the turbulent wake and the Kelvin wake correspond to dark/bright pairs. Firstly, we restrict the search area of the peak/trough pair to avoiding the influence of 'X-Lines' and search for a peak/trough pair, which refers to the turbulent wake and one of the Kelvin arms. According to Equation (1), the search window is 10° to 20°. Then, the other Kelvin arm is searched according to the detected turbulent wake. An example can be seen in Figure 6.

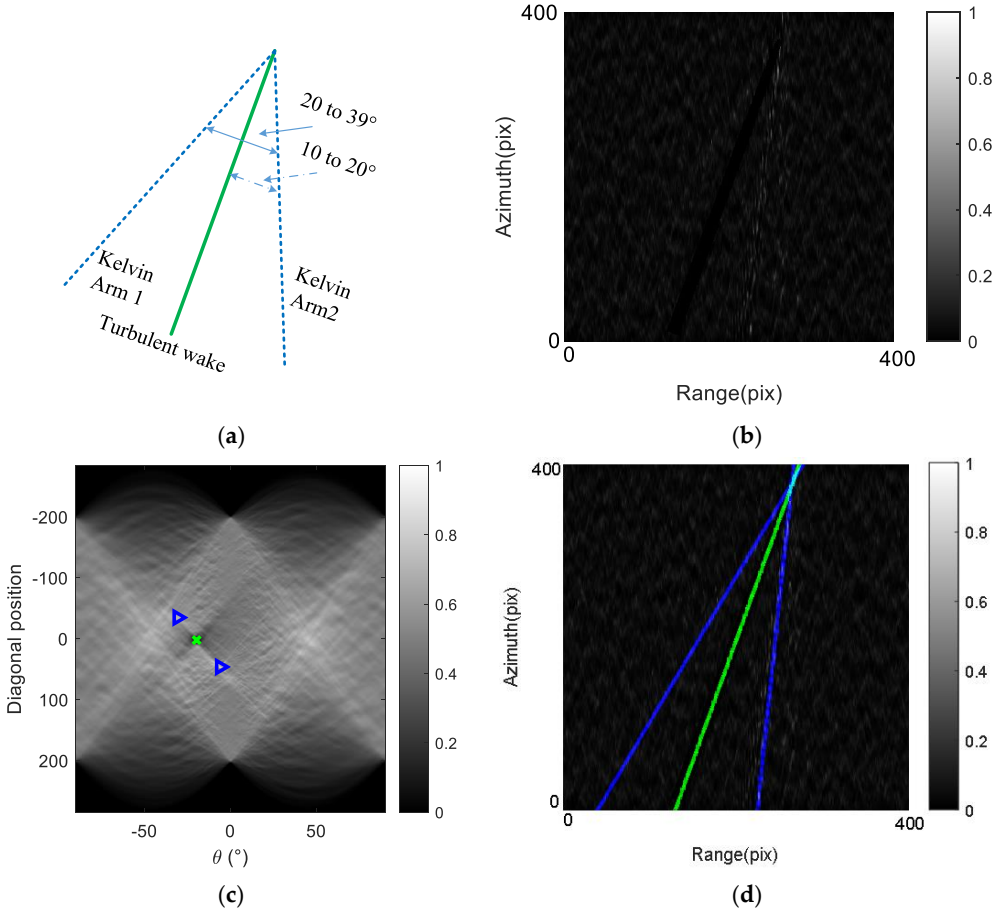


Figure 6. Detection procedure of Kelvin wake and turbulent wake in SAR images. (**a**) Diagrammatic sketch; (**b**) Simulated SAR images; (**c**) Radon images; (**d**) Detected wakes. The Kelvin wake arms are represented by the blue color, and the turbulent wake is represented by the green color.

A measure index F_I can be used to confirm the wake and it represents the difference between the average intensity over the unconfirmed wake. It is positive for bright Kelvin wakes and negative for the dark turbulent wake [29,33]. The index F_I varies with different detecting algorithms; for example, in reference [29], they assumed a margin of 10% after a trial–error procedure and $F_I < 0$ for turbulent wake and $F_I > 0.1$ for both narrow-V and Kelvin wakes. While in reference [33], the index F_I has different forms for narrow-V, Kelvin and turbulent wake: $F_I < 0$ for turbulent wake, $F_I > 0$ for narrow-V and $F_I > 0.33$ for

Kelvin wake. In this paper, we calculated the index F_I as $F_I = \overline{I_w}/\overline{I} - 1$, where $\overline{I_w}$ and $\overline{I}$ are the mean intensity of the unconfirmed wakes and the whole SAR image, respectively. And $F_I < 0$ for turbulent wake, and $F_I > 0.25$ for Kelvin wakes according to the measured and simulated SAR images in this paper.

The detecting flow chart of the whole wake detection procedure can be seen from Figure 7.

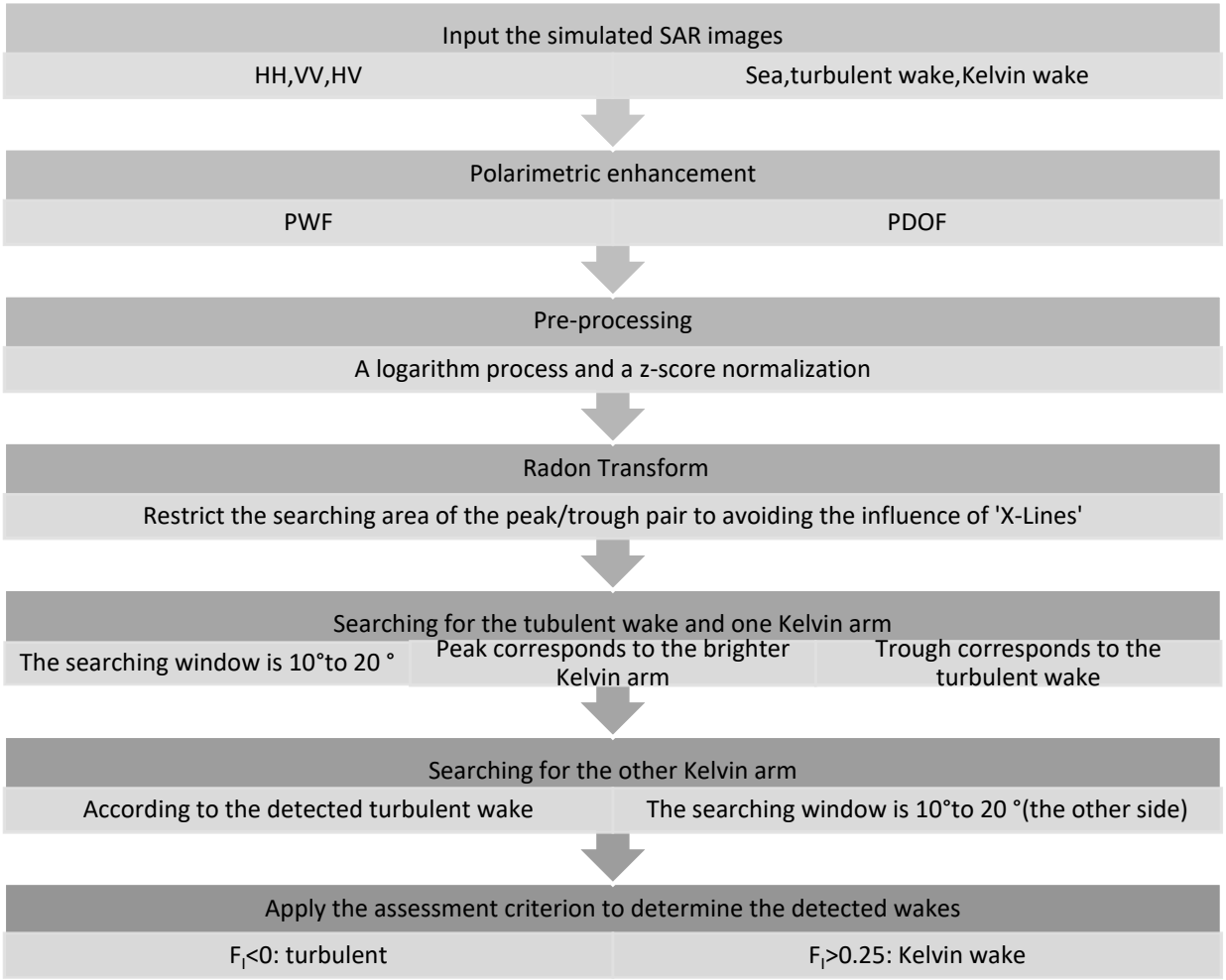


Figure 7. The detecting flow chart.

3.4. Assessment Criteria

3.4.1. Confirmation of Single Wake Character

Since there are two types of wakes to be detected in this paper, we proposed a new wake criterion to assess the performance of detecting two or more ship wakes. The detection performance analysis of each wake character is carried out independently and then combined. Then, the detection performance of detecting at least one wake type and the detection performance of detecting all the wake types can be obtained by the combination of the two. Before this, since the PMD and PFA are often used to measure the detection performances, the definition of the true detection, false detection and missed detection of the turbulent wake and Kelvin wake is crucial and should be discussed here in detail first.

Firstly, for the turbulent wake, when the angular difference of the actual/simulated and the detected wakes is below 3 degrees, the detected wakes can be confirmed. So, there three kinds of situations may exist in the detection of turbulent wake: true detection, false detection and missed detection, as shown in Figure 8. The black solid line and black dotted line represent the simulated turbulent wake and Kelvin wake, respectively; the green solid

line represents the correctly detected turbulent wake; the red solid line represents the false detected turbulent wake.

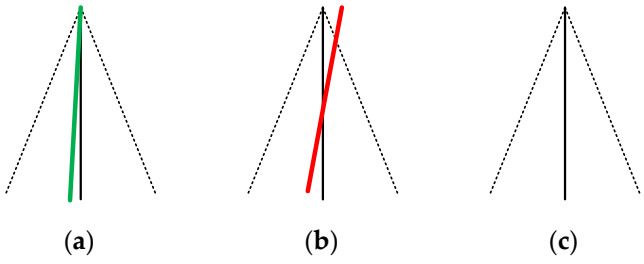


Figure 8. The detection result of the turbulent wake. (**a**) True detection; (**b**) false detection; (**c**) missed detection.

While, for the Kelvin wake detection, the situation becomes more complicated which is explained here in detail. For the Kelvin wake, apart from the 3 degrees angular difference (Kelvin restriction 2), it has to meet equation (1) (Kelvin restriction 1) before it can be confirmed. According to reference [25], when the detected V satisfies Kelvin restriction (1) and (2), it is a faithful detection; when the detected V satisfies restriction (1) but not (2), it is a false detection; when the detected V satisfies restriction (2) but not (1) or when both restriction (1) and (2) are not satisfied, it is a missed detection. However, according to the detection procedure adopted in this paper, one Kelvin wake and the turbulent wake are detected simultaneously first, and the other Kelvin wake is searched according to the detected turbulent wake, and the search window is 10° to 20°. This means the detected Kelvin wakes have already satisfied the (Kelvin restriction 1). In addition, since we use a measure index to confirm the detected wakes, there two situations may exist: both detected Kelvin wake are confirmed, and only one Kelvin wake arm is confirmed.

To sum up, there are three kinds of situations in the Kelvin wake detection: true detection, false detection, and missed detection. The true detection of Kelvin wake: two Kelvin wakes are correctly detected, and only one Kelvin wake is correctly detected. The false detection of Kelvin wake: only one Kelvin wake is wrongly detected and the other Kelvin wake is missed, one Kelvin wake is wrongly detected and the other Kelvin wake is correctly detected, two Kelvin wakes are both wrongly detected. The missed detection of Kelvin wake: two Kelvin wakes are both missed. The above situations are shown in Figure 9. The black solid line and black dotted line represent the simulated turbulent wake and Kelvin wake, respectively; the blue dashed line represents the correctly detected Kelvin wake; the red dashed line represents the false detected Kelvin wake.

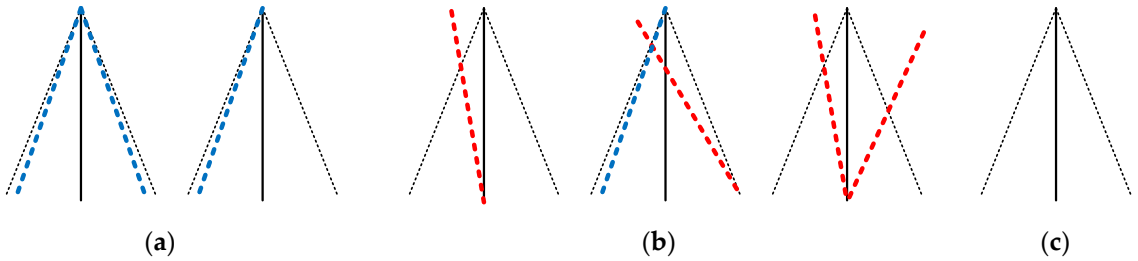


Figure 9. The detection result of the Kelvin wake. (**a**) True detection; (**b**) False detection; (**c**) Missed detection.

3.4.2. Detection Combination of the Kelvin and Turbulent Wake

The wake detection combination of the Kelvin wake and turbulent wake can be categorized by two kinds of practical requirements: detecting at least one wake type, and detecting all the wake types. The former and the latter can be seen as the loose and strict requirements of the whole detection system, which meet different practical needs. For example, the former may be suitable when the wake information is only used to assist

the search of the small and stealth ship. And the latter may be suitable for automatic ship tracking and ship parameters estimation.

To be more precise, if we introduce the *PMD* and the *PFA* to assess the detection performance, then the *PMD* and *PFA* of the Kelvin wake and the turbulent wake are calculated independently at first. The *PMD* and the *PFA* of the Kelvin wake only, turbulent wake only, and two wakes simultaneously detected are expressed by PMD_{kel}/PFA_{kel}, PMD_{tur}/PFA_{tur} and PMD_{kt}/PFA_{kt}. For each kind, assume the number of all the simulated SAR image is SN, the number of true detections is TN and the number of false detections is FN. Then, the $PMD_{tur/kel/kt}$ and the $PFA_{tur/kel/kt}$ can be calculated as follows [25]

$$PFA_{tur/kel/kt} = \frac{FN}{SN}, PMD_{tur/kel/kt} = 1 - \frac{TN}{SN}. \tag{11}$$

The PMD_t and PFA_t of detecting all the wake types can be calculated as:

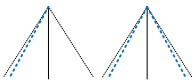
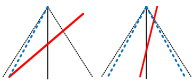
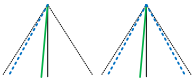
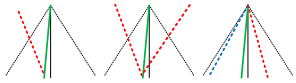
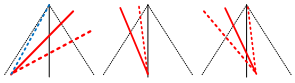
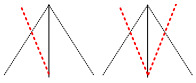
$$\begin{cases} PMD_t = PMD_{kt} \\ PFA_t = PFA_{kt} \end{cases} \tag{12}$$

The PMD_s and PFA_s of detecting at least one wake type can be calculated as:

$$\begin{cases} PMD_s = PMD_{tur} + PMD_{kel} - PMD_{kt} \\ PFA_s = PFA_{tur} + PFA_{kel} - PFA_{kt} \end{cases} \tag{13}$$

All seventeen possible wake detection scenarios of the combination of Kelvin wake and turbulent wake can be divided into nine categories according to the detection results of the two wake characters, which have been listed in Table 1.

Table 1. The possible wake detection results.

Situation Number	Figure Examples	Kelvin Detection Result	Turbulent Detection Result
1		M	T [1]
2		T	M [3]
3		T	F [2]
4		T	T
5		F	T
6		F	F
7		F	M
8		M	F
9		M	M

[1] True; [2] False; [3] Missed.

In Table 1, for each wake character, we use 'T' to represent the true detection, 'F' to represent the false detection and 'M' to represent the missed detection. The situation can occur that one kind of wake is correctly detected but the other is not. For Kelvin wake only, the true detections include situation numbers 2, 3, 4, and the false detections include situation numbers 5, 6, 7. For turbulent wake only, the true detections include situation numbers 1, 4 and 5, and the false detections include situation numbers 3, 6 and 8. For ship wake and turbulent wake simultaneously, the true detections only include situation number 4, and the false detections only include situation number 6.

4. Experiment and Discussion

4.1. Wake Detection in the Simulated SAR Images

4.1.1. The Simulated Fully Polarized SAR Images

The proposed algorithm has been applied to the simulated SAR images first. The simulation parameters of the experiment are listed in Table 2.

Table 2. The simulation parameters.

Ship Parameters	Wind-Driven Sea Parameters	SAR System Parameters
L = 52 m, B = 5.7 m, T = 3.5 m	wind speed U_{10}: 4:2:14 m/s	Airborne, H = 7000 m, V = 160 m/s
	PM spectrum	Λ = 0.031 m, SAR scene:
U_{ship}: 6:2:12 m/s	directional spreading function:	1000 m × 1000 m, resolution:
Ship heading angle: 0:10°:350°	LH, S = 7	2.5 m, radar incidence angle: 35°
	wind direction: 0°:45°:180°	polarization: HH, VV, HV

In this paper, to compare with the previous work, the parameters are partly taken from [25,26,29]. We set the ship parameters to represent a typical unmanned ship. The ship length L is 52 m, beam B is 5.7 m, draft T is 3.5 m. The ship velocity U_{ship} ranges from 6 m/s to 12 m/s with a step of 2 m/s, and ship heading angle varies from 0° to 350° with a step of 10°. For the wind-driven sea surface simulation, the wind speed at 10 m above the mean sea surface varies from 4 m/s to 14 m/s with a step of 2 m/s. The Pierson–Moskowitz (PM) spectrum [40] was adopted to simulate the omnidirectional sea wave spectrum. The corresponding significant wave height can be calculated approximately, which varies from 0.3823 m to 4.8246 m, and it covers the sea state from zero to six according to the World Meteorological Organization's definition of sea state, from calm to very rough [41]. To represent the wave directionality, the LH spreading function [42] has been adopted, and the parameter S was set to be the typical value seven. And the wind direction varies between 0° to 180° with a step of 45°. The SAR platform is chosen as the airborne, its altitude H is 7000 m and its velocity V is 160 m/s. The frequency was set to 9.65 GHz and the wavelength λ is 0.031 m. The SAR image scene is 1 km in the range direction and 1 km in the azimuth direction. The range resolution is 2.5 m, and the radar incidence angle is 35°. The polarization modes include HH, VV, HV. In such a way, for each polarization, 4320 SAR images have been simulated with Kelvin wake in them.

The simulated SAR Images of different wind speed and ship velocity have been analyzed and are listed in Figure 10. Figure 10b–x shares the same coordinates with Figure 10a. The wind direction is 0°, the ship heading angle is 0° and the polarization mode is HH. The wind speed is set to 4 m/s, 6 m/s, 8 m/s, 10 m/s, 12 m/s and 14 m/s, respectively, and the ship velocity is set to 6 m/s, 8 m/s, 10 m/s and 12 m/s, respectively. It can be seen from Figure 10 that when the wind speed is 4 m/s,6 m/s,8 m/s, 10 m/s and the significant wave height is below 3 m, as the ship velocity increases the Kelvin wake becomes more distinguishable by visual inspection. However, when the wind speed rises to 12 m/s and 14 m/s and the significant wave height is above 3 m, the Kelvin wake can hardly be distinguished from the sea clutter background by visual inspection, and increasing ship velocity still brings little effect.

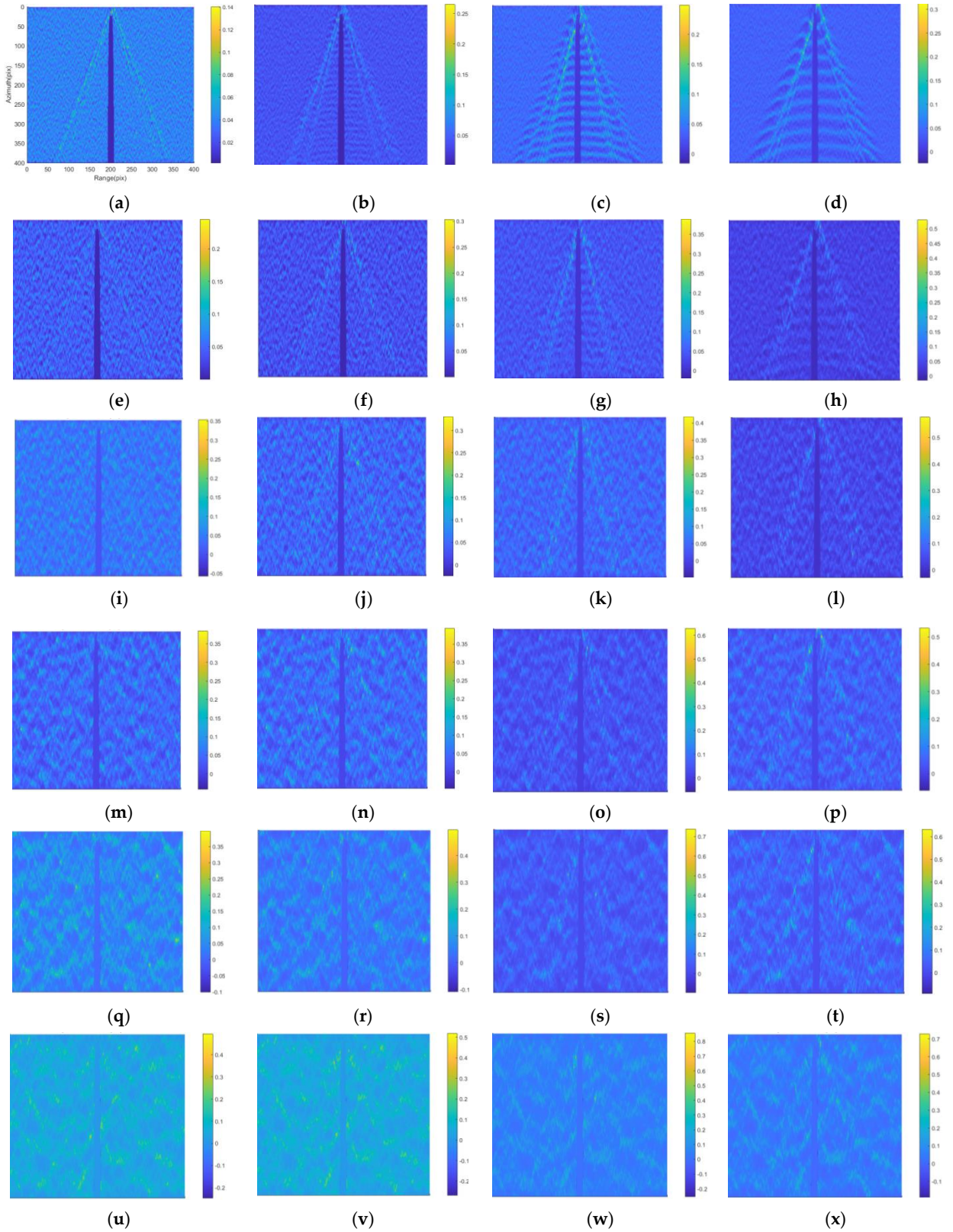
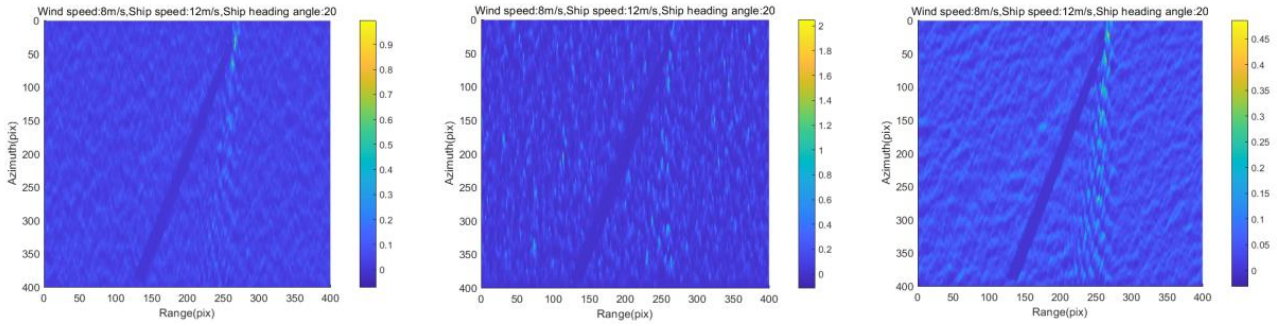


Figure 10. The simulated SAR images of different wind speed and ship velocity. (**a**–**d**) U_{10} is 4 m/s, U_{ship} is 6 m/s, 8 m/s, 10 m/s and 12 m/s; (**e**–**h**) U_{10} is 6 m/s, U_{ship} is 6 m/s, 8 m/s, 10 m/s and 12 m/s; (**i**–**l**) U_{10} is 8 m/s, U_{ship} is 6 m/s, 8 m/s, 10 m/s and 12 m/s; (**m**–**p**) U_{10} is 10 m/s, U_{ship} is 6 m/s, 8 m/s, 10 m/s and 12 m/s; (**q**–**t**) U_{10} is 12 m/s, U_{ship} is 6 m/s, 8 m/s, 10 m/s and 12 m/s; (**u**–**x**) U_{10} is 14 m/s, U_{ship} is 6 m/s, 8 m/s, 10 m/s and 12 m/s.

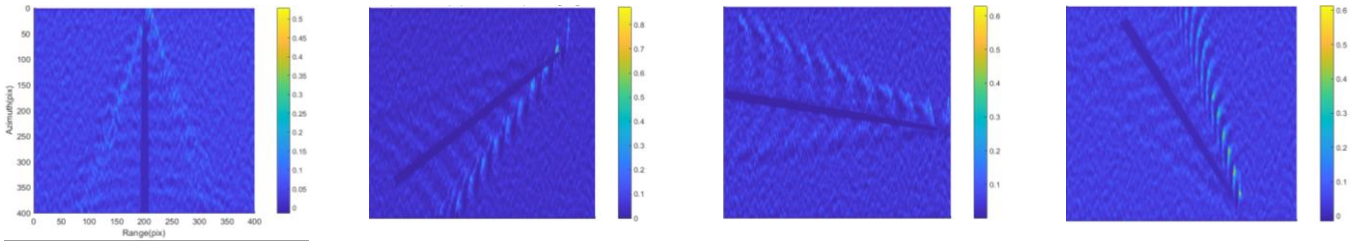
The simulated SAR images of different wind directions have been plotted in Figure 11. The wind speed is 8 m/s, the ship velocity is 12 m/s and the ship heading angle is 20°. The wind direction is 0°, 90° and 180°, respectively, and the polarization mode is HH. It can be seen that the wind direction mainly influences the sea clutter, which therefore influences the Kelvin wake arms superposed on it.



(**a**) (**b**) (**c**)

Figure 11. The simulated SAR images of different wind direction. (**a**) 0°; (**b**) 90°; (**c**) 180°.

The simulated SAR images of different ship heading angles can also be seen in Figure 12. Figure 12b–d shares the same coordinates as Figure 12a. The wind direction is 0°, the wind speed is 6 m/s and the ship velocity is 12 m/s. The ship heading angle is 0°, 50°, 100°, 150°, respectively, and the polarization mode is HH. It can be seen that, as the ship heading angle changes, the intensity difference between two Kelvin wake arms changes too. For most of the situations one arm is brighter than the other one, which may influence the confirmation of Kelvin wake.



(**a**) (**b**) (**c**) (**d**)

Figure 12. The simulated SAR images of different ship heading angles. (**a**) 0°; (**b**) 50°; (**c**) 100°; (**d**) 150°.

4.1.2. The Detection Results

After the polarimetric enhancement and the pre-process, the wake detection procedure has been carried out in the simulated SAR images of HH, VV, HV, PWF and PDOF, each including 4320 pictures, with the simulation parameters listed in Table 2.

Firstly, the influence of wind speed and wind direction on the wake detection performance with all the ship velocities considered has been analyzed. The PMD_s/PFA_s and PMD_t/PFA_t of wake detection at different wind speeds and wind directions have been counted and recorded in Table 3.

Having taken all the wind directions and ship velocities into consideration, the wake detection performances of different wind speed before and, after linear filtering, have been plotted in Figure 13. Each point represents the PMD/PFA of a certain wind speed, and each line represents the fitted results of wind speed rising from 4 m/s to 16 m/s. In this paper, the results of HH, VV, HV, PWF and PDOF are plotted using the colors blue, red, green, magenta and black. The PMD_s/PFA_s is plotted with a circle and a dotted line, and the PMD_t/PFA_t is plotted with a square and a dashed line.

Table 3. The wake detection results of different wind speed and wind direction with all the ship velocities considered.

Polarization	Wind Speed (m/s)	Wind Direction											
		0°–180°		0°		45°		90°		135°		180°	
		PMD_s	PFA_s	PMD_s	PFA_s	PMD_s	PFA_s	PMD_s	PFA_s	PMD_s	PFA_s	PMD_s	PFA_s
HH	4	0.0361	0.0569	0.0208	0.0764	0.0417	0.0625	0.0417	0.0417	0.0347	0.0486	0.0417	0.0556
	6	0.0458	0.0861	0.0208	0.06254	0.0625	0.1042	0.0625	0.1111	0.0486	0.0833	0.0347	0.0694
	8	0.0542	0.16523	0.0556	0.15248	0.05556	0.1458	0.0556	0.1875	0.0556	0.1736	0.0486	0.1667
	10	0.0694	0.2028	0.0556	0.2014	0.1181	0.2361	0.0556	0.2153	0.0486	0.1319	0.0694	0.2292
	12	0.0861	0.2986	0.0556	0.3125	0.1597	0.2500	0.0764	0.3472	0.0833	0.3194	0.0556	0.2639
	14	0.1417	0.3986	0.0556	0.4167	0.1944	0.4028	0.2569	0.4861	0.1458	0.3611	0.0556	0.3264
VV	4	0.0556	0.100	0.0556	0.1319	0.0556	0.0903	0.0556	0.0625	0.0556	0.1250	0.0556	0.0903
	6	0.0556	0.1958	0.0556	0.2222	0.0556	0.2014	0.0556	0.1528	0.0556	0.1944	0.0556	0.2083
	8	0.0569	0.2889	0.0556	0.3333	0.0625	0.22224	0.0556	0.2708	0.0556	0.2986	0.0556	0.3194
	10	0.0625	0.2958	0.0625	0.3333	0.0764	0.3056	0.0556	0.2847	0.0556	0.2292	0.0625	0.3264
	12	0.0556	0.3681	0.0556	0.3681	0.0556	0.2986	0.0556	0.3611	0.0556	0.4236	0.0556	0.3889
	14	0.0611	0.3972	0.0556	0.46523	0.0556	0.2986	0.0764	0.4653	0.0625	0.3611	0.0556	0.3958
HV	4	0.0125	0.0458	0	0.0417	0	0.0208	0.0278	0.0486	0.0069	0.0486	0.0278	0.0694
	6	0.0278	0.0556	0	0.0486	0.0347	0.0556	0.0556	0.0556	0.0417	0.0556	0.0069	0.0625
	8	0.0417	0.0681	0.0139	0.0625	0.0556	0.0694	0.0556	0.0694	0.0556	0.0833	0.0278	0.0556
	10	0.0514	0.0944	0.0556	0.0556	0.0556	0.1250	0.0556	0.1042	0.0556	0.1042	0.0347	0.0833
	12	0.0542	0.1431	0.0486	0.1042	0.0556	0.1250	0.0556	0.2292	0.0556	0.1875	0.0556	0.0694
	14	0.0569	0.1583	0.0625	0.1736	0.0556	0.1667	0.0556	0.1597	0.0556	0.1458	0.0556	0.1458
PWF	4	0.0250	0.0375	0.0139	0.0556	0.0139	0.0139	0.0486	0.0486	0.0208	0.0278	0.0278	0.0417
	6	0.0403	0.0639	0.0069	0.0486	0.0556	0.0833	0.0625	0.0833	0.0556	0.0556	0.0208	0.0486
	8	0.0458	0.0889	0.0417	0.0556	0.0486	0.0764	0.0556	0.1389	0.0486	0.1181	0.0347	0.0556
	10	0.0500	0.1361	0.0417	0.0694	0.0556	0.1458	0.0556	0.2153	0.0556	0.1667	0.0417	0.0833
	12	0.0528	0.1792	0.0556	0.1111	0.0556	0.1667	0.0556	0.2708	0.0556	0.2431	0.0417	0.1042
	14	0.0583	0.2333	0.0625	0.1597	0.0556	0.1875	0.0625	0.4028	0.0556	0.2431	0.0556	0.1736
PDOF	4	0.0083	0.0333	0	0.0278	0	0.0139	0.0347	0.0486	0	0.0278	0.0069	0.0486
	6	0.0222	0.0444	0	0.0347	0.0347	0.0556	0.0556	0.0556	0.0208	0.0208	0	0.0556
	8	0.0361	0.0611	0.0139	0.0347	0.0556	0.0625	0.0556	0.1042	0.0556	0.0625	0	0.0417
	10	0.0444	0.0778	0.0417	0.0556	0.0556	0.0764	0.0556	0.0972	0.0556	0.0903	0.0139	0.0694
	12	0.0486	0.1167	0.0486	0.0694	0.0556	0.1250	0.0556	0.2014	0.0556	0.1111	0.0278	0.0764
	14	0.0569	0.1472	0.0625	0.0764	0.0486	0.1528	0.0556	0.2083	0.0625	0.1319	0.0556	0.1667

Polarization	Wind speed (m/s)	Wind Direction											
		0°–180°		0°		45°		90°		135°		180°	
		PMD_t	PFA_t	PMD_t	PFA_t	PMD_t	PFA_t	PMD_t	PFA_t	PMD_t	PFA_t	PMD_t	PFA_t
HH	4	0.0986	0.0361	0.1042	0.0208	0.1042	0.0417	0.1319	0.0417	0.0764	0.0347	0.0764	0.0417
	6	0.1514	0.0444	0.0694	0.0208	0.1736	0.0625	0.2569	0.0556	0.1806	0.0486	0.0764	0.0347
	8	0.2347	0.0528	0.1667	0.0486	0.2569	0.0556	0.3333	0.0556	0.2361	0.0556	0.1806	0.0486
	10	0.3069	0.0694	0.2153	0.0556	0.3681	0.1181	0.4236	0.0556	0.2847	0.0486	0.2431	0.0694
	12	0.3736	0.0861	0.3125	0.0556	0.4097	0.1597	0.4722	0.0764	0.3889	0.0833	0.2847	0.0556
	14	0.4542	0.1417	0.4167	0.0556	0.5000	0.1944	0.5625	0.2569	0.4653	0.1458	0.3264	0.0556
VV	4	0.2083	0.0556	0.2014	0.0556	0.1736	0.0556	0.2986	0.0556	0.2153	0.0556	0.1528	0.0556
	6	0.2847	0.0556	0.2569	0.0556	0.2986	0.0556	0.3403	0.0556	0.3125	0.0556	0.2153	0.0556
	8	0.3514	0.0569	0.3472	0.0556	0.3472	0.0625	0.3889	0.0556	0.3542	0.0556	0.3194	0.0556
	10	0.3903	0.0625	0.3403	0.0625	0.4514	0.0764	0.4792	0.0556	0.3333	0.0556	0.3472	0.0625
	12	0.4236	0.0556	0.3750	0.0556	0.4167	0.0556	0.4653	0.0556	0.4722	0.0556	0.3889	0.0556
	14	0.4694	0.0611	0.4722	0.0556	0.4028	0.0556	0.6319	0.0764	0.4306	0.0625	0.4097	0.0556
HV	4	0.0500	0.0125	0.0486	0	0.0278	0	0.0556	0.0278	0.0486	0.0069	0.0694	0.0278
	6	0.0653	0.0250	0.0486	0	0.0694	0.0347	0.0903	0.0556	0.0556	0.0278	0.0625	0.0069
	8	0.0972	0.0417	0.0625	0.0139	0.1042	0.0556	0.1597	0.0556	0.1042	0.0556	0.0556	0.0278
	10	0.1417	0.0486	0.0556	0.0486	0.1597	0.0556	0.2361	0.0556	0.1736	0.0486	0.0833	0.0347
	12	0.2083	0.0542	0.1250	0.0486	0.2361	0.0556	0.3472	0.0556	0.2639	0.0555	0.0694	0.0556
	14	0.2319	0.0542	0.1875	0.0625	0.2500	0.0556	0.3452	0.0417	0.2222	0.0556	0.1458	0.0556
PWF	4	0.0375	0.0236	0.0556	0.0139	0.0139	0.0069	0.0486	0.0486	0.0278	0.0208	0.0417	0.0278
	6	0.0750	0.0361	0.0486	0.0069	0.0833	0.0556	0.1389	0.0486	0.0556	0.0486	0.0486	0.0208
	8	0.1250	0.0458	0.0625	0.0417	0.1250	0.0486	0.2361	0.0556	0.1458	0.0486	0.0556	0.0347
	10	0.1972	0.0500	0.0694	0.0417	0.2361	0.0556	0.3472	0.0556	0.2500	0.0556	0.0833	0.0417
	12	0.2139	0.0528	0.1250	0.0556	0.2500	0.0556	0.3194	0.0556	0.2708	0.0556	0.1042	0.0417
	14	0.2875	0.0569	0.1597	0.0625	0.2500	0.0556	0.5556	0.0556	0.2986	0.0556	0.1736	0.0556

Table 3. *Cont.*

PDOF	4	0.0375	0.0069	0.0278	0	0.0139	0	0.0694	0.0278	0.0278	0	0.0486	0.0069
	6	0.0764	0.0153	0.0347	0	0.0694	0.0208	0.1736	0.0417	0.0486	0.0139	0.0556	0
	8	0.1333	0.0236	0.0347	0.0139	0.1597	0.0347	0.2917	0.0486	0.1319	0.0208	0.0486	0
	10	0.1625	0.0264	0.0556	0.0278	0.2083	0.0347	0.2708	0.0278	0.2014	0.0278	0.0764	0.0139
	12	0.2028	0.0417	0.0903	0.0417	0.3056	0.0556	0.3264	0.0417	0.2153	0.0417	0.0764	0.0278
	14	0.2556	0.0486	0.0972	0.0625	0.2847	0.0486	0.4306	0.0278	0.2917	0.0486	0.1736	0.0556

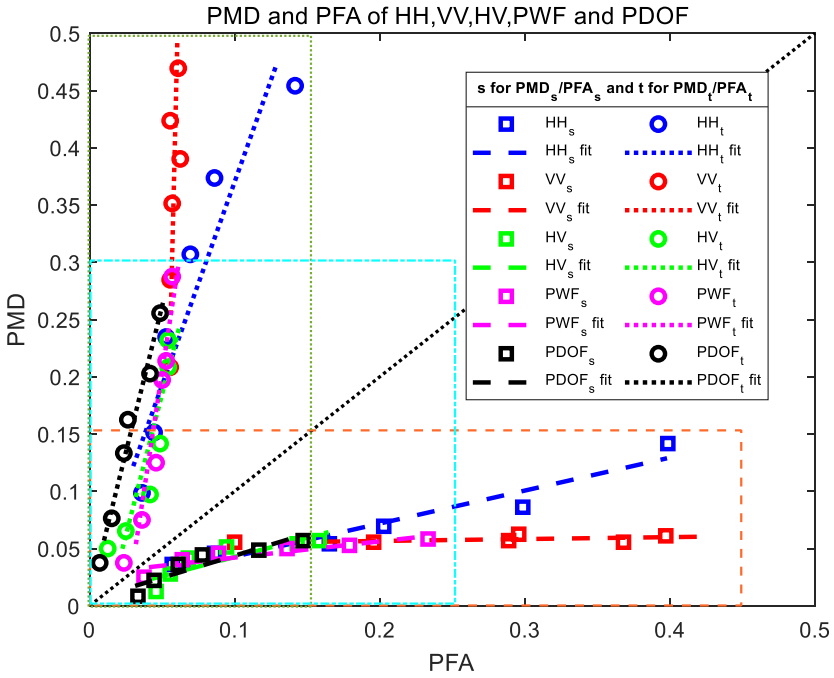


Figure 13. The wake detection performances of different wind speed before and after linear filtering with all ship velocities, ship heading angles and wind directions considered. The PMD/PFA range of [0:0.15, 0:0.45], [0:0.5, 0:0.15] and [0:0.3, 0:0.25] are represented by the dashed, dotted and dash–dot line squares.

As seen in Table 3 and Figure 13, the wind speed has quite different influences on the PMD and PFA for the two different detection requirements. When all the ship velocities are taken into consideration, the distribution range of PMD_s/PFA_s is about [0:0.15, 0:0.45], and the distribution range of PMD_t/PFA_t is about [0:0.5, 0:0.15]. For HH, VV, HV, PWF and PDOF, as the wind speed increases from 4 m/s to 14 m/s, the PMD_s/PFA_s rises from 0.0361/0.0569, 0.0556/0.100, 0.0125/0.0458, 0.0250/0.0375, 0.0083/0.0333 to 0.1417/0.3986, 0.0611/0.3972, 0.0569/0.1583, 0.0583/0.2333, 0.0569/0.1472, respectively, and the PMD_t/PFA_t changes from 0.0986/0.0361, 0.2083/0.0556, 0.0500/0.0125, 0.0375/0.0236, 0.0375/0.0069 to 0.4542/0.1417, 0.4694/0.0611, 0.2319/0.0542, 0.2875/0.0569, 0.2556/0.0486, respectively. The PMD_s/PFA_s and PMD_t/PFA_t are distributed mainly in [0:0.3, 0:0.25] for PWF, PDOF and HV, but for HH and VV this range becomes [0:0.5, 0:0.5].

The influence of wind direction on the wake detection performance with all the ship velocities considered has been analyzed too, which varies from 0° to 180° with a step of 45°. The PMD_s/PFA_s and PMD_t/PFA_t of different wind speed have been counted and displayed in Figure 14, with each subfigure representing a certain wind speed and each point representing the PMD/PFA of a certain wind direction. It can be seen that the change in wind direction influences the PMD/PFA for both HH, VV, HV, PWF and PDOF. We use the cyan dash–dotted lines to show the PMD/PFA distribution range of HV, PDOF and PWF, which can represent the different sensitivity to wind direction. As seen from Figure 14d, taking all the wind speeds into consideration, the PMD/PFA of HV, PDOF and PWF are mainly distributed in [0:0.28, 0:0.15], but for HH and VV it is [0:0.45, 0:0.35]. When

the wind speed is 6, 10, 14 m/s, the distribution ranges of PMD/PFA of HV, PDOF and PWF are nearly [0:0.08, 0:0.08], [0:0.3, 0:0.2], [0:0.45, 0:0.25], respectively, except for some error points.

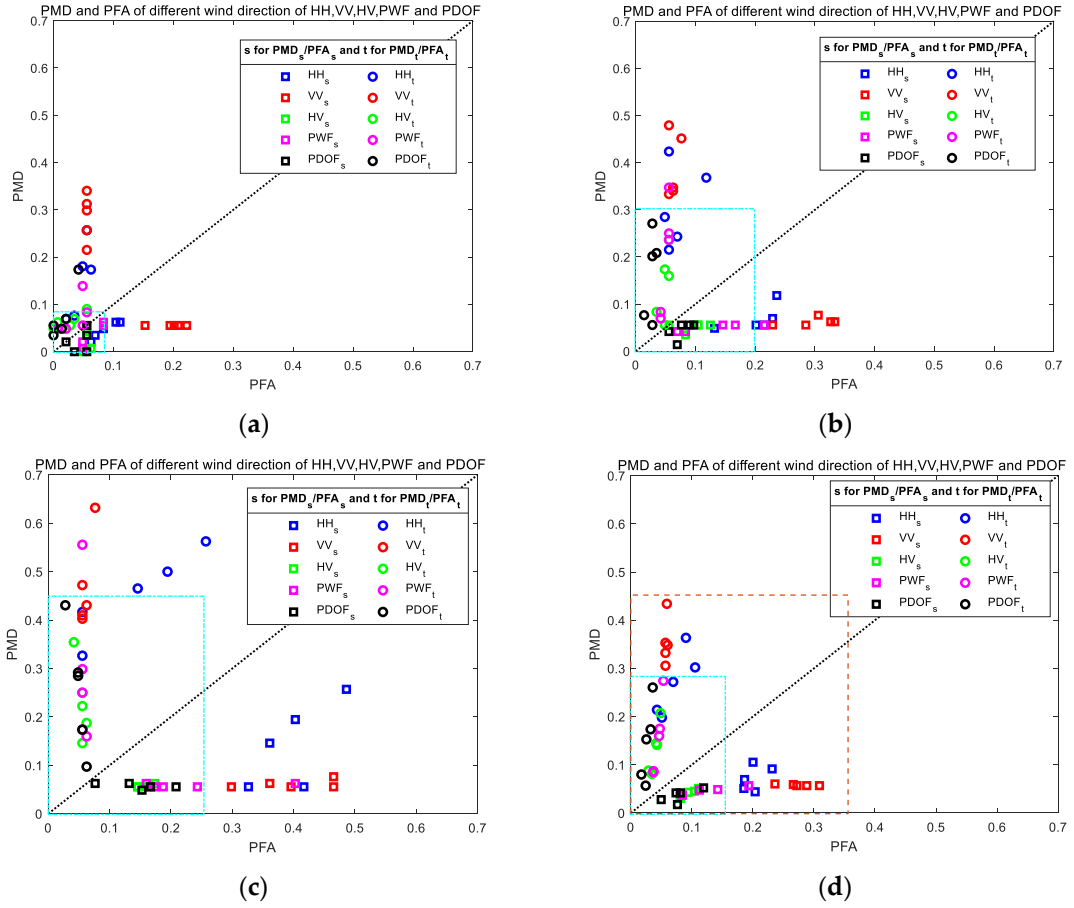


Figure 14. The wake detection performances of different wind direction under different wind speeds. (**a**) Wind speed 6 m/s; (**b**) 10 m/s; (**c**) 14 m/s; (**d**) 4–14 m/s. The PMD/PFA range of [0:0.08, 0:0.08], [0:0.3, 0:0.2], [0:0.45, 0:0.25] and [0:0.28, 0:0.15] are represented by the dash–dot line squares in (**a**–**d**). The PMD/PFA range of [0:0.45, 0:0.35] is represented by the dashed line square in (**d**).

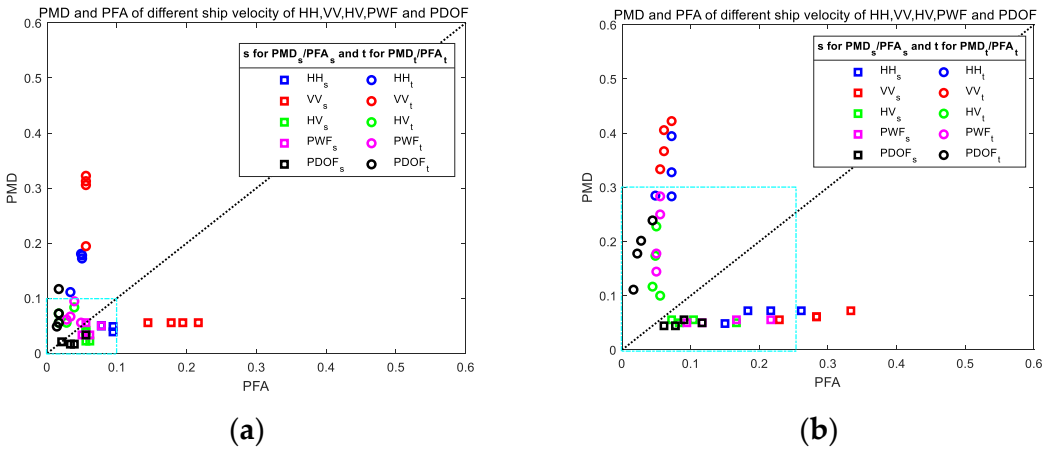
We also analyzed the influence of ship velocity on the wake detection performance, which varies from 6 m/s to 12 m/s with a step of 2 m/s for all the wind directions considered. The PMD_s/PFA_s and PMD_t/PFA_t of different ship velocity have been counted and displayed in Table 4 and Figure 15, with each subfigure representing a different wind speed and each point representing the PMD/PFA of a certain ship velocity. Taking all the wind speeds and directions into consideration, when the ship velocity rises from 6 m/s to 12 m/s, the PMD_t/PFA_t of HH, VV, HV, PWF and PDOF changes from 0.3176/0.0778, 0.3676/0.0620, 0.1824/0.0361, 0.1981/0.0463, 0.2204/0.0324 to 0.2213/0.0639, 0.3630/0.0565, 0.1157/0.0380, 0.1417/0.0463, 0.1046/0.0241, respectively. When the wind speed is 6, 10, 14 m/s, the distribution ranges of PMD/PFA of HV, PDOF and PWF are nearly [0:0.1, 0:0.1], [0:0.3, 0:0.25], [0:0.4, 0:0.35] except for some error points. When all the wind speeds are taken into consideration, the PMD/PFA of HV, PDOF and PWF are distributed mainly in [0:0.2, 0:0.2].

We also analyzed the influence of ship heading angle on the wake detection performance, which varies from 0° to 350° with a step of 10°, with all the ship velocities considered. The PMD_s/PFA_s and PMD_t/PFA_t of different wind speeds have been counted and displayed in Figure 16, with each subfigure representing a different wind speed and each point representing a certain ship heading angle. Seen from Figure 16a–c that as the wind

speed increases, the number of wrong detection points increases too. Seen from Figure 16d that when all the wind speeds are taken into consideration, wrong detections are very likely to occur for ship heading angles 90° and 270°, denoted by a dash–dot line square.

Table 4. The wake detection performances of different ship velocities and wind speeds with all the wind directions considered.

Polarization	U_{10} (m/s)	Ship Velocity (m/s)															
		6				8				10				12			
		PMD_s	PFA_s	PMD_t	PFA_t	PMD_s	PFA_s	PMD_t	PFA_t	PMD_s	PFA_s	PMD_t	PFA_t	PMD_s	PFA_s	PMD_t	PFA_t
HH	4	0.017	0.039	0.083	0.017	0.022	0.050	0.056	0.022	0.044	0.072	0.150	0.044	0.061	0.067	0.106	0.061
	6	0.050	0.078	0.172	0.050	0.039	0.094	0.111	0.033	0.050	0.078	0.178	0.050	0.044	0.094	0.144	0.044
	8	0.050	0.222	0.300	0.050	0.056	0.167	0.200	0.056	0.056	0.161	0.278	0.050	0.056	0.111	0.161	0.056
	10	0.072	0.261	0.394	0.072	0.072	0.217	0.283	0.072	0.072	0.183	0.328	0.072	0.061	0.150	0.222	0.061
	12	0.100	0.367	0.428	0.100	0.083	0.272	0.344	0.083	0.094	0.306	0.406	0.094	0.067	0.250	0.317	0.067
	14	0.178	0.489	0.528	0.178	0.183	0.439	0.483	0.183	0.111	0.356	0.428	0.111	0.094	0.311	0.378	0.094
VV	4	0.056	0.072	0.133	0.056	0.056	0.094	0.156	0.056	0.056	0.072	0.256	0.056	0.056	0.161	0.289	0.056
	6	0.056	0.217	0.306	0.056	0.056	0.144	0.194	0.056	0.056	0.178	0.322	0.056	0.056	0.244	0.317	0.056
	8	0.056	0.311	0.306	0.056	0.056	0.283	0.322	0.056	0.056	0.294	0.383	0.056	0.061	0.267	0.344	0.061
	10	0.072	0.333	0.422	0.072	0.061	0.283	0.367	0.061	0.061	0.283	0.406	0.061	0.056	0.283	0.367	0.056
	12	0.056	0.411	0.456	0.056	0.056	0.372	0.411	0.056	0.056	0.333	0.428	0.056	0.056	0.356	0.400	0.056
	14	0.078	0.478	0.533	0.078	0.056	0.394	0.439	0.056	0.056	0.356	0.444	0.056	0.056	0.361	0.461	0.056
HV	4	0.006	0.044	0.044	0.006	0.017	0.044	0.050	0.017	0.017	0.044	0.056	0.017	0.011	0.050	0.050	0.011
	6	0.023	0.061	0.072	0.017	0.022	0.056	0.056	0.017	0.039	0.056	0.083	0.039	0.028	0.050	0.050	0.028
	8	0.039	0.078	0.133	0.039	0.044	0.061	0.078	0.044	0.044	0.061	0.078	0.044	0.039	0.072	0.100	0.039
	10	0.050	0.167	0.228	0.050	0.056	0.072	0.100	0.056	0.050	0.083	0.117	0.044	0.050	0.056	0.122	0.044
	12	0.056	0.194	0.278	0.056	0.056	0.133	0.189	0.056	0.056	0.117	0.167	0.056	0.050	0.128	0.200	0.050
	14	0.056	0.250	0.339	0.050	0.056	0.167	0.228	0.050	0.061	0.117	0.189	0.061	0.056	0.100	0.172	0.056
PWF	4	0.028	0.033	0.033	0.028	0.017	0.039	0.039	0.017	0.022	0.028	0.028	0.017	0.033	0.050	0.050	0.033
	6	0.050	0.078	0.094	0.039	0.033	0.061	0.067	0.033	0.033	0.050	0.061	0.028	0.044	0.067	0.078	0.044
	8	0.039	0.128	0.156	0.039	0.044	0.078	0.122	0.044	0.050	0.072	0.106	0.050	0.050	0.078	0.117	0.050
	10	0.056	0.217	0.283	0.056	0.050	0.117	0.178	0.005	0.050	0.094	0.144	0.050	0.044	0.117	0.183	0.044
	12	0.056	0.228	0.250	0.056	0.056	0.150	0.183	0.056	0.050	0.183	0.222	0.050	0.050	0.156	0.200	0.050
	14	0.061	0.317	0.372	0.061	0.056	0.261	0.322	0.056	0.056	0.172	0.233	0.056	0.061	0.183	0.222	0.056
PDOF	4	0.0056	0.039	0.050	0	0.0056	0.017	0.022	0.006	0.017	0.050	0.050	0.017	0.006	0.028	0.028	0.006
	6	0.017	0.039	0.117	0.017	0.017	0.033	0.056	0.017	0.033	0.056	0.072	0.017	0.022	0.050	0.061	0.011
	8	0.033	0.078	0.211	0.022	0.033	0.050	0.128	0.022	0.039	0.050	0.089	0.022	0.039	0.067	0.106	0.028
	10	0.050	0.117	0.239	0.044	0.044	0.078	0.178	0.022	0.044	0.061	0.111	0.017	0.039	0.056	0.122	0.022
	12	0.050	0.189	0.317	0.044	0.044	0.094	0.172	0.039	0.050	0.089	0.161	0.039	0.050	0.094	0.161	0.044
	14	0.078	0.228	0.389	0.067	0.061	0.172	0.272	0.056	0.039	0.089	0.211	0.039	0.050	0.100	0.150	0.033



(**a**) (**b**)

Figure 15. *Cont.*

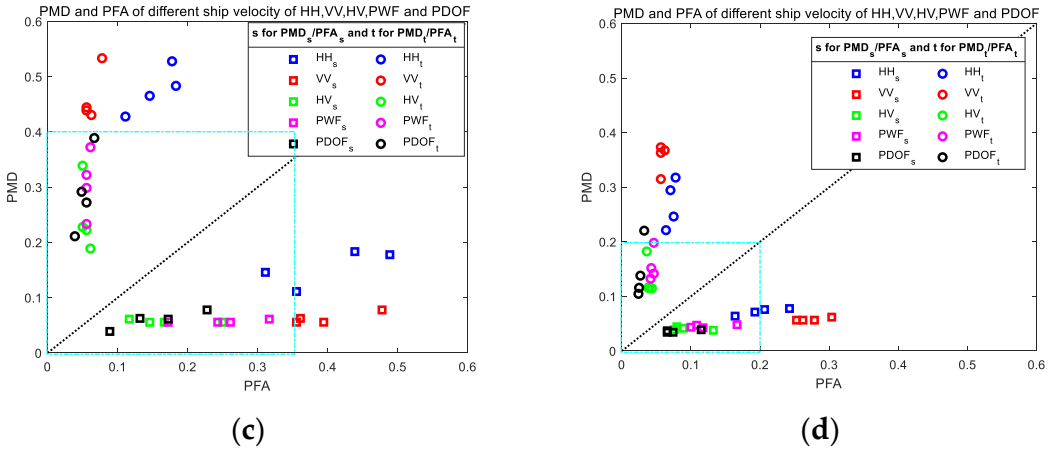


Figure 15. The wake detection performances of different ship velocity under different wind speeds. (**a**) Wind speed 6 m/s; (**b**) 10 m/s; (**c**) 14 m/s; (**d**) 4–14 m/s. The PMD/PFA range of [0:0.1, 0:0.1], [0:0.3, 0:0.25], [0:0.4, 0:0.35] and [0:0.2, 0:0.2] are represented by the dash–dot line squares in (**a**–**d**).

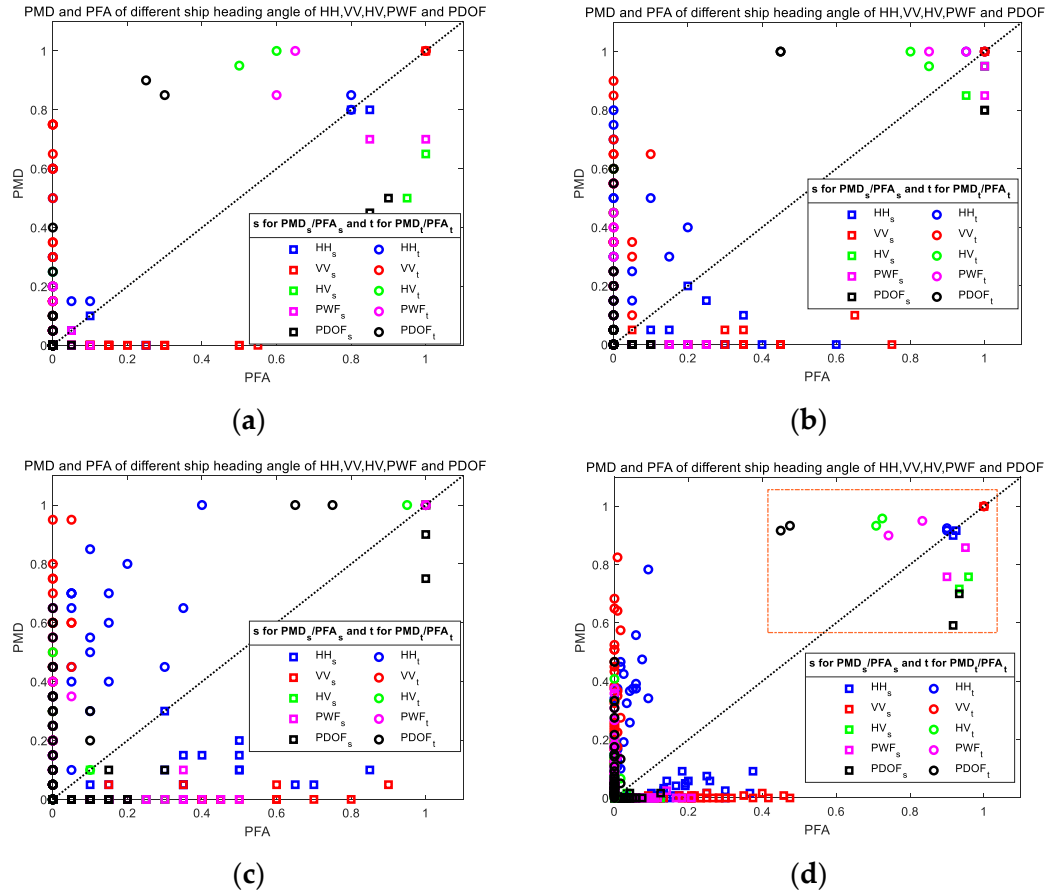


Figure 16. The wake detection performances of different ship heading angle under different wind speeds. (**a**) Wind speed 6 m/s; (**b**) 10 m/s; (**c**) 14 m/s; (**d**) 4–14 m/s. The wrong detections denoted by a dash–dot line square in (**d**).

4.2. Wake Detection in the Measured SAR Images

To solve the lack of the public dataset, reference [27] recently presented a public Fully Polarized Ship Detection Dataset (FPSD) for the first time, which contains 853 Pauli pseudo-color maps (in JPG format) and multilook complex data (in TIF format), with a total of 1714 ship targets from AIRSAR, UAVSAR, and RadarSAT-2. Pixel-level annotation based on Pauli pseudo-color maps was performed using the open-source software LabelMe

for annotation purposes. In this paper, three kinds of typical measured fully polarized SAR data have been selected from the FPSD to verify the ship wake detection algorithms by visual inspection and the annotations, representing the situation of wake character as easy (00150), hard (00466) and very hard (00234) to be distinguished from the sea clutter background. And their Pauli pseudo-color maps and the annotations have been displayed in Figure 17. Since the prior information of the ship parameters is hard to obtain in the measured data, the wake detection procedure has been only carried out in the measured HH, VV, HV and PWF SAR images in this paper.

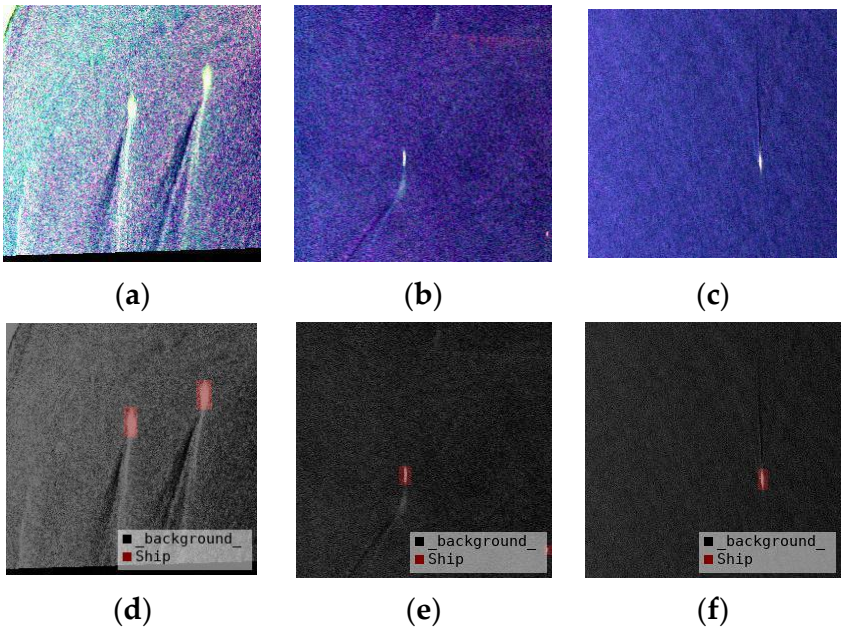


Figure 17. The Pauli pseudo-color maps and the ship annotations of the selected three data. (**a**) Pauli pseudo-color map of data 00150; (**b**) Pauli pseudo-color map of data 00466; (**c**) Pauli pseudo-color map of data 00234; (**d**) Ship annotation of data 00150; (**e**) Ship annotation of data 00466; (**f**) Ship annotation of data 00234.

The detection results for data 00150 are shown in Figure 18, and the Kelvin wakes can be correctly detected in both HH, VV, HV and PWF SAR images. Actually, there are two obvious ships and their wakes in the image, but only the brighter ship wakes are detected here. As seen from the results, the turbulent and two Kelvin wakes have been detected and confirmed correctly for HH, VV and PWF. And the turbulent and both Kelvin wake have been detected for HV, but one Kelvin arm has not been confirmed. Both four detection results correspond to situation 4 in Table 1 and can be considered as true detections for both Kelvin and turbulent wake.

The turbulent wake character of data 00466 is relatively clear from visual inspection, but the Kelvin wake can hardly be seen. In addition, there is less wake information compared with data 00150 and the main component is the sea clutter background. Therefore, a certain area needs to be chosen from the original SAR images, which mainly includes the possible wake areas. In this paper, this area contains 150 pixels in range and azimuth direction. The detection results are shown in Figure 19, and for PWF SAR images, the turbulent wake and both Kelvin wake arms can be correctly detected and confirmed. For HH, HV the turbulent and both Kelvin wakes have been detected but only the turbulent and one Kelvin wake arm have been confirmed. In VV SAR images the turbulent wake has been wrongly detected, and only one Kelvin wake arm has been correctly detected and confirmed.

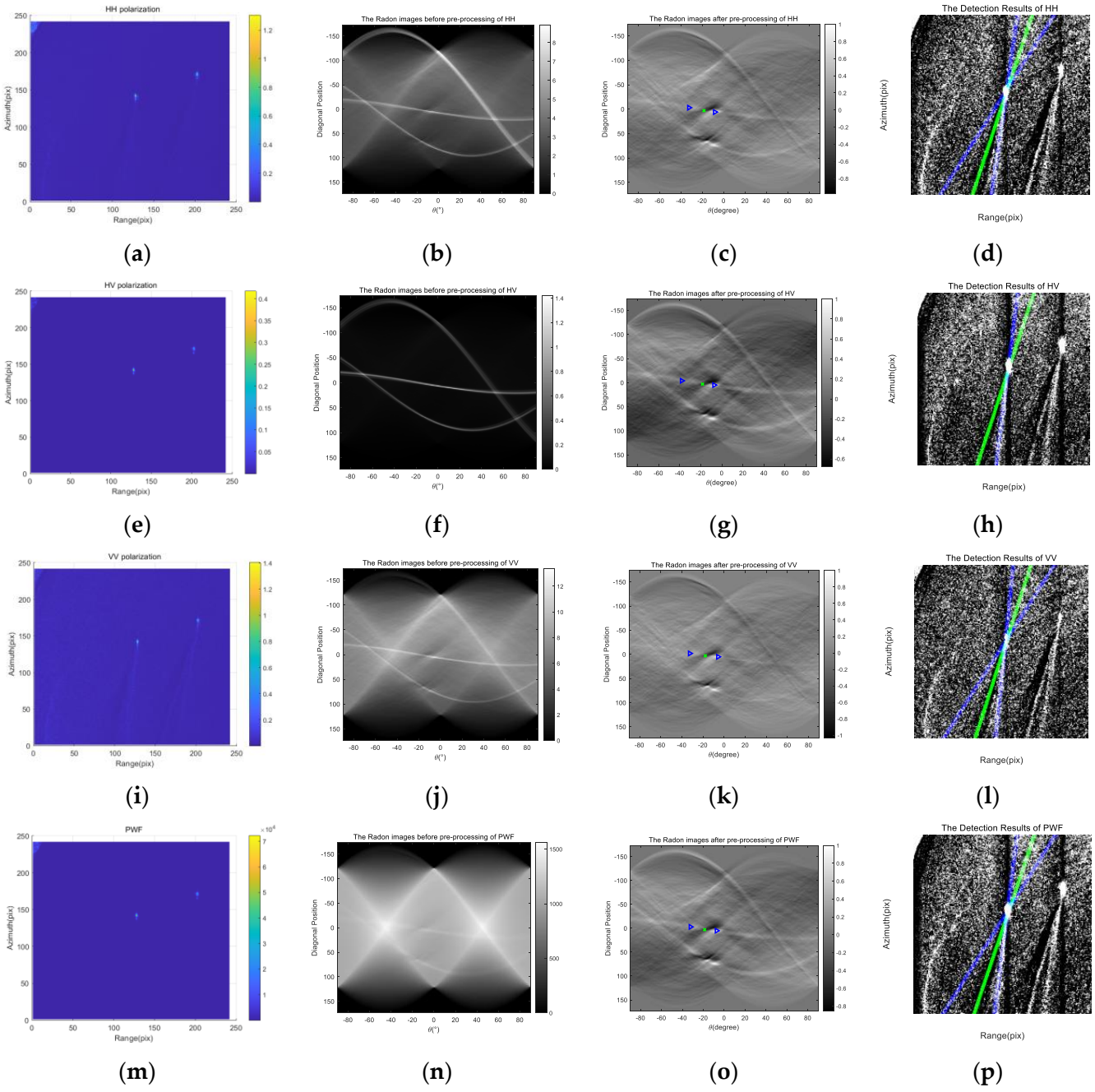
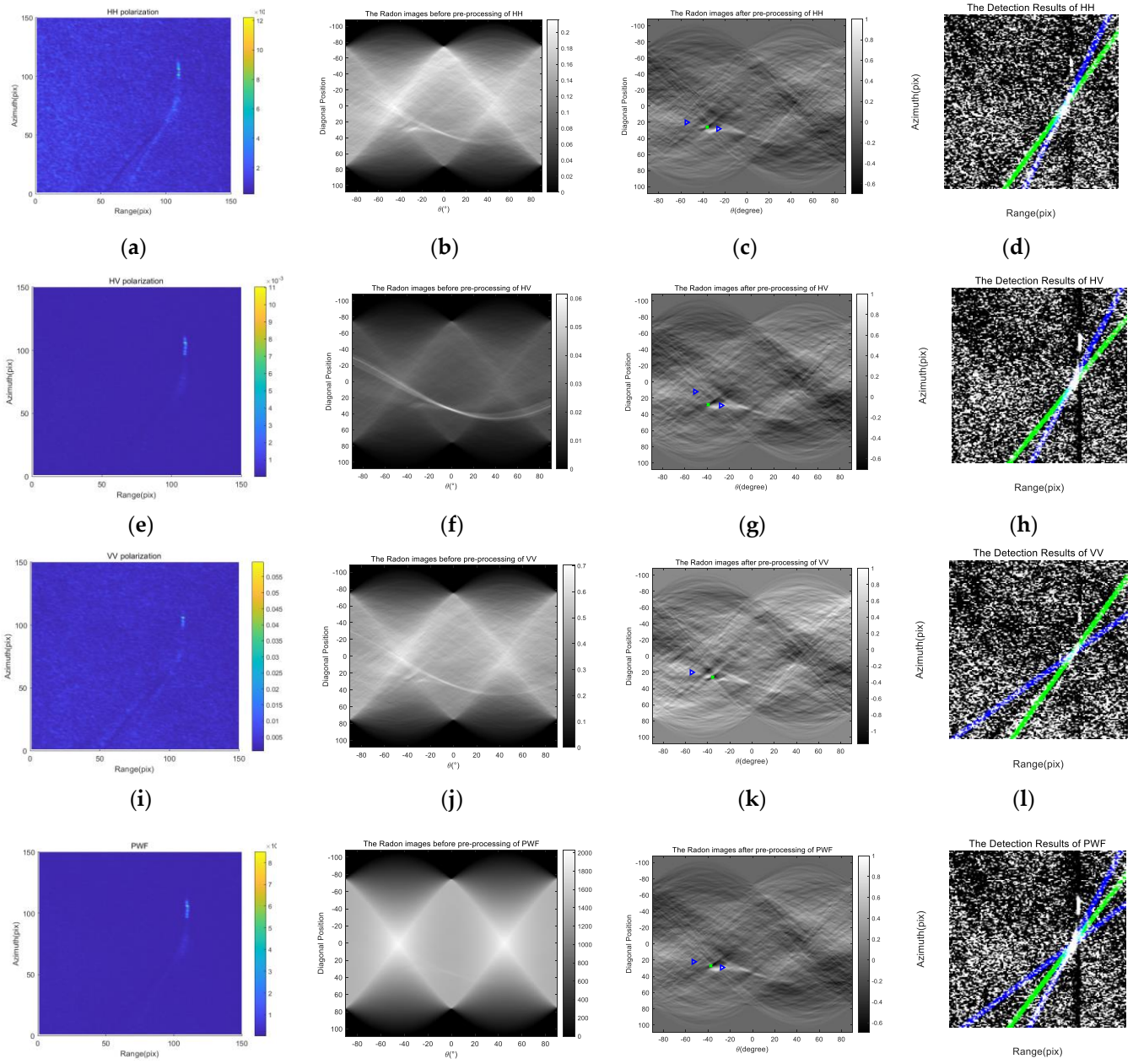


Figure 18. Detection results for data 00150. (**a**,**e**,**i**,**m**) SAR images of HH, HV, VV, PWF; (**b**,**f**,**j**,**n**) Radon images of HH, HV, VV, PWF; (**c**,**g**,**k**,**o**) Radon images of HH, HV, VV, PWF after pre−processing and detection results; (**d**,**h**,**l**,**p**) detection results of HH, HV, VV, PWF.

As for figure number 00234, both the turbulent and the Kelvin wakes are very faint and certain areas needs to be cut from the SAR images, which mainly includes the possible wake areas and contains 180 pixels in range and azimuth direction. The detection results from data 00234 have been shown in Figure 20, and all three wakes can be correctly detected and confirmed in VV SAR images, the turbulent and both Kelvin wakes have been detected but only the turbulent and one Kelvin wake arm have been confirmed in HV and PWF images. But in HH SAR images the turbulent wake has been wrongly detected, and only one Kelvin wake arm has been correctly detected and confirmed.



(**a**) (**b**) (**c**) (**d**)

(**e**) (**f**) (**g**) (**h**)

(**i**) (**j**) (**k**) (**l**)

(**m**) (**n**) (**o**) (**p**)

Figure 19. Detection results for data 00466. (**a**,**e**,**i**,**m**) SAR images of HH, HV, VV, PWF; (**b**,**f**,**j**,**n**) Radon images of HH, HV, VV, PWF; (**c**,**g**,**k**,**o**) Radon images of HH, HV, VV, PWF after pre−processing and detection results; (**d**,**h**,**l**,**p**) Detection results of HH, HV, VV, PWF.

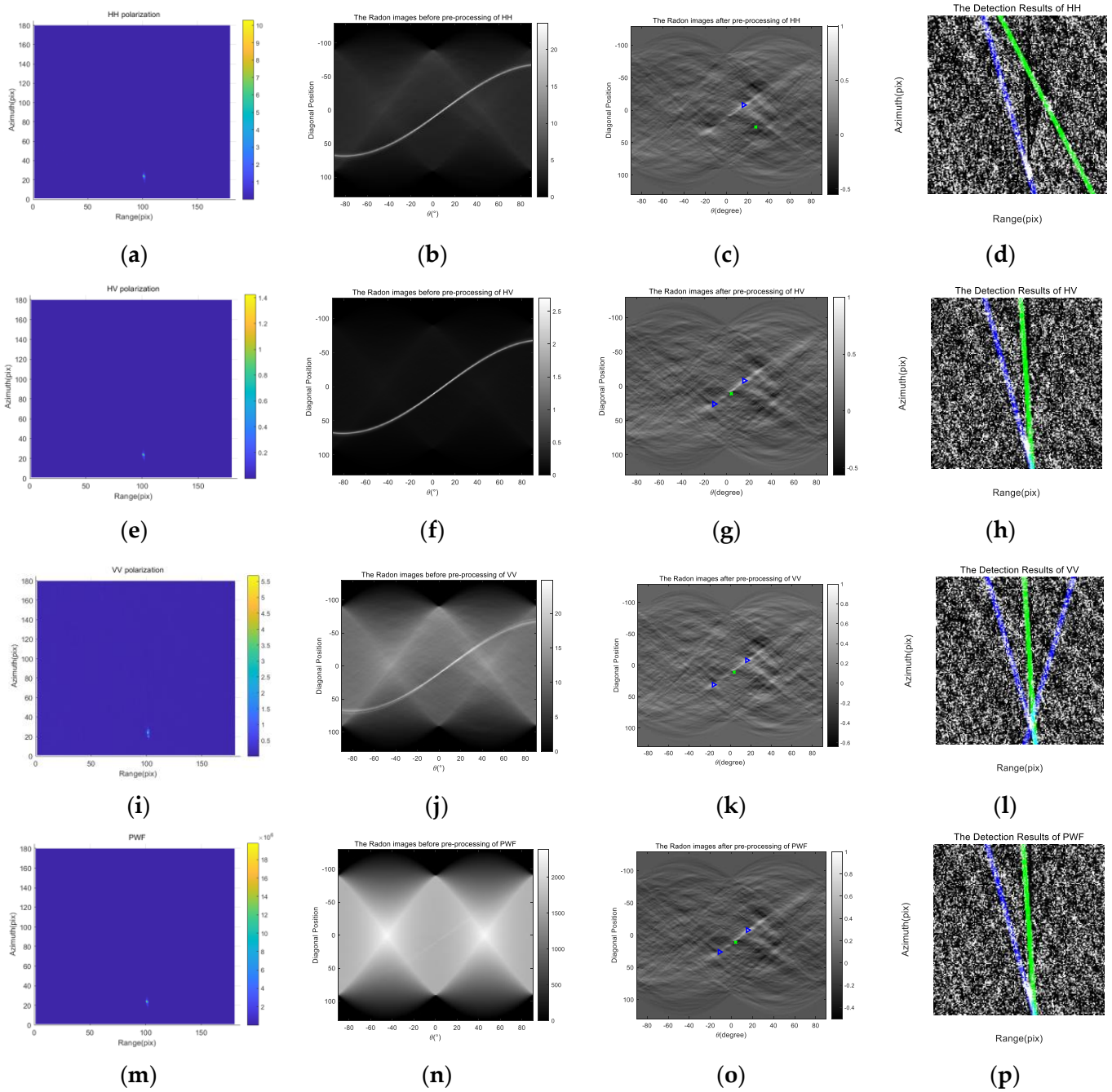


Figure 20. Detection results for data 00234. (**a**,**e**,**i**,**m**) SAR images of HH, HV, VV, PWF; (**b**,**f**,**j**,**n**) Radon images of HH, HV, VV, PWF; (**c**,**g**,**k**,**o**) Radon images of HH, HV, VV, PWF after pre−processing and detection results; (**d**,**h**,**l**,**p**) Detection results of HH, HV, VV, PWF.

4.3. Discussion

As can be seen from the simulated SAR imagery, for the simulation parameters listed in Table 2, when the wind speed exceeds 12 m/s, the Kelvin wake can hardly be distinguished from the sea clutter background by visual inspection, and increasing ship velocity brings little effect. Take the HH polarization for example, as the wind speed increases from 4 m/s to 14 m/s, the PMD_s/PFA_s rises from 0.0361/0.0569 to 0.1417/0.3986 and the PMD_t/PFA_t rises from 0.0986/0.0361 to 0.4542/0.1417. This indicates that it is necessary to adopt polarimetric enhancement methods to improve the ship wake detection of small ships during the high state. After the polarimetric enhancement process, the ship wake character can be effectively enhanced. The PWF can effectively suppress the sea clutter, and the

PDOF can suppress the sea clutter as well as enhance the target information. However, the dark turbulent wake becomes almost invisible after PWF and PDOF, and sometimes some singular points exist which may cause wake misdetection. The PWF and PDOF also enlarge the intensity difference of SAR imagery of HH, VV, HV, PWF and PDOF. For both the simulated and measured SAR images, the image intensity of PFOF is about ten thousand times higher than that of PWF, a million times higher than that of HH and VV and a hundred million times higher than that of HV.

Since we mainly detected the ship wakes in the Radon images in this paper, the bright and singular points resulting from the ship echoes and the polarimetric enhancement measures may easily lead to the misdetection of ship wake. A logarithm process and a z-score normalization have been proposed to eliminate the uniformity of HH, VV, HV, PWF and PDOF, as well as the influence of the singular points. After the pre-process, all the image intensities obey a Gauss distribution for both the simulated and measured data, and the influences of the singular points have been reduced. A Radon transform-based ship wake detection algorithm and a new assessment criterion have been applied to the simulated and measured SAR images, composed of the confirmation of single wake character and the combination of the Kelvin and turbulent wake. Since the measured data contain 4320 SAR images for the HH, VV, HV, PWF and PDOF, the PMD_s/PFA_s and the PMD_t/PFA_t can be used to characterize the wake detection performances for statistical purpose, which stands for the situation of detecting at least one wake type and detecting all the wake types. For the former situation, wrongly detecting simply one wake will cause a false alarm, therefore the false alarms tend to be easier (higher PFA). And for the latter situation, it is a missing detection unless both the two wakes are correctly detected, therefore the missing detections tend to be easier (higher PMD). For example, the distribution range of PMD_s/PFA_s and PMD_t/PFA_t is about [0:0.15, 0:0.45] and [0:0.5, 0:0.15] in Figure 13. Then, the algorithm was applied to three kinds of typically measured fully polarized SAR data selected from the FPSD by visual inspection and the annotations, and the detection results have verified the correctness of the algorithm described in this paper.

The influences of wind speed, wind direction, ship velocity and ship heading angle on the wake detection performance have been analyzed in detail for the simulated images. The wind speed is a determining influencing factor, and the increase in wind speed worsens the wake detection performances of both HH, VV, HV, PWF and PDOF, illustrated by Table 3 and Figure 13. The PMD_s/PFA_s and PMD_t/PFA_t versus the wind direction do not obey a linear relation. And the detection performances of HH and VV are more sensitive to the change in wind direction, as illustrated by Table 3 and Figure 14. This can be explained by the fact that both the PWF and PDOF apply the average value of the selected clutter region to suppress sea clutter, and the sea clutter of cross-polarization has been suppressed. The increase in ship velocity reduces the PMD/PFA for both HH, VV, HV, PWF and PDOF in general, resulting in an obvious improvement, illustrated by Table 4 and Figure 15. Greater ship velocity produces more obvious wake characters, therefore the ship wake detection becomes easier. The ship heading angle of 90° and 270° are likely to cause misdetection in this paper.

Furthermore, the detection performance of PWF, PDOF and HV outperforms that of HH and VV, which is clearly denoted by the distribution ranges of the PMD_s/PFA_s and PMD_t/PFA_t in Figures 13–16. And the wake detection performances of PWF and PDOF are better than that of HH and VV, HV is slightly better than PWF, and PDOF is the best of all. This is because the PWF and PDOF have utilized the full-polarimetric SAR signatures of ocean surface features and ship wakes, and the wake detection performance can be effectively improved after the polarimetric enhancement. Compared with the previous wake detection results, which are is also based on the simulated SAR imagery [25] and the HH and VV polarization, for rough sea with significant wave height is about 4 m, the corresponding PMD and PFA of ship Kelvin wake detection may reach 0.5 and 0.2, correspondingly. In this paper, it is reasonable to compare the detection performances of the detecting all the types of wake situations to make a comparison with [25]. When the wind

speed reaches 14 m/s and the significant wave height is about 5 m, the PMD_t/PFA_t of HH, VV, HV, PWF and PDOF are 0.4542/0.1417, 0.4694/0.0611, 0.2319/0.0542, 0.2875/0.0569, 0.2556/0.0486, correspondingly. The detecting performance in this paper is slightly better for HH and VV, and is much better for HV, PWF and PDOF than in [25].

5. Conclusions

In this paper, the fully polarized SAR imagery of ship turbulent wake and ship Kelvin wake has been simulated, and the polarimetric enhancement methods including the PWF and PDOF have been applied to enhance the wake features in the PolSAR imagery. After a logarithm process and a z-score normalization pre-processing, the uniformity of the intensity of HH, VV, HV, PWF and PDOF imagery has been eliminated and the influences of the bright and singular points resulted from the ship echoes and the polarimetric enhancement methods have been reduced. A new assessment criterion for wake detection performance has been formulated, and then a Radon transform-based ship wake detection algorithm has been carried out for these SAR images. The wake detection results show that PWF and PDOF can improve the wake detection performance by an average of nearly 50 percent compared with the HH and VV in similar previous algorithms, and the detection performance of PDOF is the best.

Future work will mainly focus on the following three aspects:

(1) Based on the ship wake detection results, ship parameters such as ship velocity, ship heading angle and ship beam can be estimated. For different ship parameters, the wake character to be enhanced is different, and the choice of prior information of the wakes is different. In the following research, more experiments need to be carried out focusing on the choose of $\mathbf{\Sigma}_T$ of the PDOF according to different situations. And deep learning algorithms need to be applied to the search of $\mathbf{\Sigma}_T$.

(2) The detection performance in this paper is carried out mainly based on a large amount of simulated SAR images, and the correctness of our algorithms can be validated through the comparison of the previous similar work. The next step is to apply this algorithm to more measured SAR imagery and assess and optimize the algorithm.

(3) The algorithm presented in this paper is also adaptable to the dual-pol and compact hybrid-pol scenarios [43,44], except for that only part of the information of the polarimetric covariance matrices will remain. And it is a special case of the fully polarized scenario. Therefore, the potential of dual-pol and compact hybrid-pol SAR needs to be further discovered.

Author Contributions: Conceptualization, T.L. and Y.J.; methodology, Y.J.; software, Y.J.; validation, T.L., Y.J. and Z.Y.; formal analysis, Y.J. and K.L.; investigation, Y.J.; resources, T.L. and K.L.; data curation, Y.J.; writing—original draft preparation, Y.J. and Z.Y.; writing—review and editing, Y.J.; visualization, Y.J.; supervision, T.L.; project administration, T.L.; funding acquisition, T.L. All authors have read and agreed to the published version of the manuscript.

Funding: This research was funded by the National Natural Science Foundation of China under Grant 62171452, 61771483.

Data Availability Statement: The data presented in this study are available on request from the corresponding author. The data are not publicly available due to privacy.

Acknowledgments: The authors would like to thank all the anonymous reviewers. Their constructive comments to improve the paper are greatly appreciated. The authors would like to thank Oktay Karakus and Alin Achim for their Matlab progamms "AssenSAR Image Simulator" and "AssenSAR-Wake-Detector-master".

Conflicts of Interest: The authors declare no conflicts of interest.

References

1. Tings, B. Non-Linear modeling of detectability of ship wake components in dependency to influencing parameters using spaceborne X-Band SAR. *Remote Sens.* **2021**, *13*, 165. [CrossRef]
2. Schuler, D.L.; Lee, J.S.; Hoppel, K.; Valenzuela, G.R. Polarimetric SAR Image Signatures of Gulf-stream Features and Ship Wakes. In Proceedings of the 1992 IEEE International Geoscience and Remote Sensing Symposium, Houston, TX, USA, 26–29 May 1992.
3. Pottier, E.; Boerner, W.M.; Schuler, D.L. Schuler Polarimetric Detection and Estimation of Ship Wakes. In Proceedings of the 1999 IEEE International Geoscience and Remote Sensing Symposium, Hamburg, Germany, 28 June–2 July 1999.
4. Kasilingam, D.; Schuler, D.; Lee, J.S.; Malhotra, S. Modulation of Polarimetric Coherence by Ocean Features. In Proceedings of the 2002 IEEE International Geoscience and Remote Sensing Symposium, Toronto, ON, Canada, 24–28 June 2002.
5. Morris, J.; Anderson, S.; Parfitt, A. Polarimetric Mapping of Ship Wakes. In Proceedings of the 2002 IEEE International Geoscience and Remote Sensing Symposium, Toronto, ON, Canada, 24–28 June 2002.
6. Morris, J.; Anderson, S. An Entropy-based Approach to Wake Echo Analysis [ship wake radar detection]. In Proceedings of the 2003 International Conference on Radar, Adelaide, Australia, 3–5 September 2003.
7. Yang, J.; Huang, W.; Xiao, Q.; Fu, B.; Yao, L. Optimal Polarization for the Observation of Ocean Features with SAR. In Proceedings of the 2004 IEEE International Geoscience and Remote Sensing Symposium, Anchorage, AL, USA, 20–24 September 2004.
8. Wu, P.; Wang, J.; Wang, W.; Sun, J. Polarimetric Characters Extraction Research of Kelvin Wakes on PolSAR Image. In Proceedings of the 2011 International Conference on Remote Sensing, Environment and Transportation Engineering, Nanjing, China, 24–26 June 2011.
9. Novak, L.M.; Sechtin, M.B.; Cardullo, M.J. Studies of target detection algorithms that use polarimetric radar data. *IEEE Trans. Aerosp. Electron. Syst.* **1989**, *25*, 150–165. [CrossRef]
10. Novak, L.M.; Burl, M.C. Optimal speckle reduction in polarimetric SAR imagery. *IEEE Trans. Aerosp. Electron. Syst.* **1990**, *26*, 293–305. [CrossRef]
11. Marino, A. A notch filter for ship detection with polarimetric SAR data. *IEEE J. Sel. Top. Appl. Earth Obs. Remote Sens.* **2013**, *6*, 1219–1232. [CrossRef]
12. Novak, L.M.; Burl, M.C.; Irving, W.W.; Owirka, G.J. Optimal Polarimetric Processing for Enhanced Target Detection. In Proceedings of the 1991 National Telesystems Conference, Atlanta, AL, USA, 23–24 March 1991.
13. Imbo, P.; Souyris, J.C.; Yeremy, M. Wake Detection in Polarimetric SAR Images. In Proceedings of the 2001 IEEE International Geoscience and Remote Sensing Symposium, Sydney, Australia, 9–13 July 2001.
14. Xu, Z.; Tang, B.; Cheng, S. Faint ship wake detection in PolSAR images. *IEEE Trans. Geosci. Remote Sens.* **2018**, *15*, 1055–1059. [CrossRef]
15. Biondi, F. Low-rank plus sparse decomposition and localized radon transform for ship-wake detection in synthetic aperture radar images. *IEEE Geosci. Remote Sens. Lett.* **2018**, *15*, 117–121. [CrossRef]
16. Biondi, F. A polarimetric extension of low-rank plus sparse decomposition and radon transform for ship wake detection in synthetic aperture radar images. *IEEE Geosci. Remote Sens. Lett.* **2019**, *16*, 75–79. [CrossRef]
17. Liu, T.; Jiang, Y.; Marino, A.; Gao, G.; Yang, J. The Polarimetric detection optimization filter and its statistical test for ship detection. *IEEE Trans. Geosci. Remote Sens.* **2022**, *60*, 1–18. [CrossRef]
18. Liu, T.; Zhang, J.; Gao, G.; Yang, J.; Marino, A. CFAR ship detection in polarimetric synthetic aperture radar images based on whitening filter. *IEEE Trans. Geosci. Remote Sens.* **2020**, *58*, 58–81. [CrossRef]
19. Liu, T.; Yang, Z.; Marino, A.; Gao, G.; Yang, J. PolSAR ship detection based on neighborhood polarimetric covariance matrix. *IEEE Trans. Geosci. Remote Sens.* **2021**, *59*, 4874–4887. [CrossRef]
20. Liu, T.; Yang, Z.; Gao, G.; Marino, A.; Chen, S.W.; Yang, J. A general framework of polarimetric detectors based on quadratic optimization. *IEEE Trans. Geosci. Remote Sens.* **2022**, *60*, 5237418. [CrossRef]
21. Liu, T.; Yang, Z.; Gao, G.; Marino, A.; Chen, S.W. Simultaneous diagonalization of Hermitian matrices and its application in PolSAR ship detection. *IEEE Trans. Geosci. Remote Sens.* **2023**, *61*, 5220818. [CrossRef]
22. Liu, T.; Tang, T.; Yang, Z.; Jiang, Y. L-distribution for multilook polarimetric SAR data and its application in ship detection. *Sci. China Inf. Sci.* **2021**, *12*, 226–238.
23. Deng, Y.; Zhang, M.; Jiang, W.; Wang, L. Electromagnetic scattering of near-field turbulent wake generated by accelerated propeller. *Remote Sens.* **2021**, *13*, 5178. [CrossRef]
24. Wang, J.; Guo, L.; Wei, Y.; Chai, S. Study on ship Kelvin wake detection in numerically simulated SAR images. *Remote Sens.* **2023**, *15*, 1089. [CrossRef]
25. Zilman, G.; Zapolski, A.; Marom, M. On detectability of a ship's kelvin wake in simulated sar images of rough sea surface. *IEEE Trans. Geosci. Remote Sens.* **2015**, *53*, 609–619. [CrossRef]
26. Rizaev, I.G.; Karakuş, O.; Hogan, S.J.; Achim, A. Modeling and SAR imaging of the sea surface: A review of the state-of-the-art with simulations. *ISPRS J. Photogramm. Remote Sens.* **2022**, *187*, 120–140. [CrossRef]
27. Yang, Z.; Zhang, P.; Wang, N.; Liu, T. A lightweight theory driven network and its validation on public fully polarized ship detection dataset. *IEEE J. Sel. Top. Appl. Earth Obs. Remote Sens.* **2024**, *17*, 3755–3767. [CrossRef]
28. Tings, B. Extension of ship wake detectability model for non-linear influences of parameters using satellite based X-band synthetic aperture radar. *Remote Sens.* **2019**, *11*, 563. [CrossRef]

29. Karakuş, O.; Rizaev, I.; Achim, A. Ship wake detection in SAR images via sparse regularization. *IEEE Trans. Geosci. Remote Sens.* **2020**, *58*, 1665–1677. [CrossRef]
30. Tings, B.; Pleskachevsky, A.; Wiehle, S. Comparison of detectability of ship wake components between C-Band and X-Band synthetic aperture radar sensors operating under different slant ranges. *ISPRS J. Photogramm. Remote Sens.* **2023**, *196*, 306–324. [CrossRef]
31. Ermakov, S.; Kapustin, I.; Lazareva, T. Ship Wake Signatures in Radar/Optical Images of the Sea Surface: Observations and Physical Mechanisms. In Proceedings of the SPIE Remote Sensing of the Ocean, Sea Ice, Coastal Waters, and Large Water Regions 2014, Amsterdam, The Netherland, 24–25 September 2014.
32. Rey, M.T.; Tunaley, J.K.; Folinsbee, J.T.; Jahans, P.A.; Dixon, J.A.; Vant, M.R. Application of Radon transform techniques to wake detection in Seasat-A SAR Images. *IEEE Trans. Geosci. Remote Sens.* **1990**, *28*, 553–560. [CrossRef]
33. Graziano, M.D.; D'Errico, M.; Rufino, G. Wake component detection in X-Band SAR images for ship heading and velocity estimation. *Remote Sens.* **2016**, *8*, 498. [CrossRef]
34. Melsheimer, C.; Lim, H.; Shen, C. Observation and Analysis of Ship Wakes in ERS SAR and SPOT Images. In Proceedings of the 20th Asian Conference on Remote Sensing, Hong Kong, China, 22–25 November 1999.
35. Zilman, G.; Zapolski, A.; Marom, M. The speed and beam of a ship from its wake's SAR images. *IEEE Trans. Geosci. Remote Sens.* **2003**, *42*, 2335–2343. [CrossRef]
36. Ren, W.J.; Liu, P.; Ren, X.C.; Jin, Y.Q. SAR image simulation of ship turbulent wake using semi-empirical energy spectrum. *IEEE J. Multiscale Multiphys Comput. Techn.* **2021**, *6*, 1–7. [CrossRef]
37. Milgram, J.H.; Skop, R.A.; Peltzer, R.D.; Griffin, O.M. Modeling short sea wave energy distribution in the far wakes of ships. *J. Geophys. Res.* **1993**, *98*, 7115–7124. [CrossRef]
38. Alpers, W.R.; Ross, D.B.; Rufenach, C.L. On the detectability of ocean surface waves by real and synthetic aperture radar. *J. Geophys. Res.* **1981**, *86*, 6481–6498. [CrossRef]
39. Lyzenga, D.R. Numerical simulation of synthetic aperture radar image spectra for ocean waves. *IEEE Trans. Geosci. Remote Sens.* **1986**, *6*, 863–872. [CrossRef]
40. Pierson, W.J.; Moskowitz, L. A proposed spectral from fully developed wind seas based on the similarity theory of SA kitaigorod-srii. *J. Geophys. Res.* **1964**, *69*, 5181–5190. [CrossRef]
41. Ward, K.; Tough, R.; Watts, S. *Sea Clutter: Scattering, the K Distribution and Radar Performance*, 2nd ed.; The Institution of Engineering and Technology: London, UK, 2013; pp. 19–21.
42. Jiang, Y.; Chen, Z.; Zhao, C. Research on Key Issues of Extracting Wind Direction from HF Surface Wave Radar Oceanic Backscatter. In Proceedings of the 2016 CIE International Conference on Radar, Guangzhou, China, 10–13 October 2016.
43. Espeseth, M.M.; Brekke, C.; Anfinsen, S.N. Hybrid-polarity and reconstruction methods for sea ice with L- and C-band SAR. *IEEE Geosci. Remote Sens. Lett.* **2016**, *13*, 467–471. [CrossRef]
44. Kumar, A.; Mishra, V.; Panigrahi, R.K.; Martorella, M. Application of hybrid-pol SAR in oil-spill detection. *IEEE Geosci. Remote Sens. Lett.* **2023**, *20*, 1–5. [CrossRef]

Disclaimer/Publisher's Note: The statements, opinions and data contained in all publications are solely those of the individual author(s) and contributor(s) and not of MDPI and/or the editor(s). MDPI and/or the editor(s) disclaim responsibility for any injury to people or property resulting from any ideas, methods, instructions or products referred to in the content.